Optimisation of the marine Nd isotope scheme in the ocean component of the FAMOUS general circulation model

Suzanne Robinson[1], Ruza Ivanovic[1], Lauren Gregoire[1], Lachlan Astfalck[2], Tina van de Flierdt[3], Yves Plancherel[3], Frerk Pöppelmeier[4], Kazuyo Tachikawa[5]

[1]School of Earth and Environment, University of Leeds, Leeds, LS2 9JT, UK
[2]School of Physics, Mathematics and Computing, The University of Western Australia, Crawley, Western Australia, Australia
[3]Department of Earth Science and Engineering, Imperial College London, London, SW7 2AZ, UK
[4]Climate and Environmental Physics, Physics Institute and Oeschger Center for Climate Change Research, University of Bern, 3012 Bern, Switzerland
[5]Aix Marseille Univ, CNRS, IRD, INRAE, Coll France, CEREGE, Aix-en-Provence, France

Correspondence to: Suzanne Robinson (ee14s2r@leeds.ac.uk)

Abstract

The neodymium (Nd) isotope composition (ε_{Nd}) of seawater can be used to trace large-scale ocean circulation features. Yet, due to the elusive nature of marine Nd cycling, particularly in discerning non-conservative particle-seawater interactions, there remains considerable uncertainty surrounding a complete description of marine Nd budgets. Here, we present an optimisation of the Nd isotope scheme within the fast coupled atmosphere-ocean general circulation model (FAMOUS), using a statistical emulator to explore the parametric uncertainty and optimal combinations of three key model inputs relating to: (1) the efficiency of reversible scavenging, (2) the magnitude of the seafloor benthic flux, and (3) a riverine source scaling, accounting for release of Nd from river sourced particulate material. Furthermore, a suite of sensitivity tests provide insight on the regional mobilisation and spatial extent (i.e., testing a margin-constrained versus a seafloor-wide benthic flux) of certain reactive sediment components. In the calibrated scheme, the global marine Nd inventory totals 4.27×10^{12} g and has a mean residence time of 727 years. Atlantic Nd isotope distributions are represented well, and the weak sensitivity of North Atlantic Deep Water to highly unradiogenic sedimentary sources implies an abyssal benthic flux is of secondary importance in determining the water mass ε_{Nd} properties under the modern vigorous circulation condition. On the other hand, Nd isotope distributions in the North Pacific are 3 to 4 ε_{Nd}-units too unradiogenic compared to water measurements, and our simulations indicate that a spatially uniform flux of bulk sediment ε_{Nd} does not sufficiently capture the mobile sediment components interacting with seawater. Our results of sensitivity tests suggest that there are distinct regional differences in how modern seawater acquires its ε_{Nd} signal, in part relating to the complex interplay of Nd addition and water advection.

1 Introduction

Neodymium (Nd) isotope variations in modern seawater broadly correlate with water mass provenance, geometry and mixing (Tachikawa et al., 2017; Goldstein and Hemming, 2003). This has resulted in the exploitation of Nd isotopes as a geochemical tracer of ocean circulation in the past and present (e.g. Lambelet et al., 2016; Lacan and Jeandel, 2005a;

35 Lippold et al., 2016; Piotrowski et al., 2012; van de Flierdt and Frank, 2010; Frank, 2002; Gutjahr et al., 2008; Piotrowski et al., 2004; Roberts et al., 2010; Howe et al., 2017; Basak et al., 2015; Dausmann et al., 2017; Hu and Piotrowski, 2018; Jonkers et al., 2015; Wilson et al., 2015; Xie et al., 2014; Pöppelmeier et al., 2020b, 2022; Blaser et al., 2019b; Goldstein and Hemming, 2003). With specific regard to the radiogenic properties of this rare earth element, its isotope composition is typically expressed in epsilon (ε_{Nd}) units, where $\varepsilon_{Nd}=[(^{143}Nd/^{144}Nd)_{sample}/(^{143}Nd/^{144}Nd)_{CHUR}-1] \times 10^4$, thus describing the parts

40 per 10,000 deviation of a sample from the chondritic uniform reservoir (CHUR) (Jacobsen and Wasserburg, 1980). Owing to somewhat poorly constrained input and output fluxes, the estimated mean ocean residence time of Nd ranges between 360-800 years (Arsouze et al., 2009; Rempfer et al., 2011; Gu et al., 2019; Pöppelmeier et al., 2020a), which is less than the global thermohaline overturning circulation time (i.e., < 1,500 years). The measured Nd isotope composition of seawater is not actively involved in marine biological cycling (Blaser et al., 2019a).

Neodymium enters the ocean in dissolved and particulate phases through continental weathering via rivers and aeolian dust deposition (Frank, 2002; Goldstein and Hemming, 2003; Grousset et al., 1998; Rousseau et al., 2015; Goldstein and Jacobsen, 1987, 1988; Rahlf et al., 2020, 2021), alongside particle-seawater exchange occurring along the sediment-water boundary (Abbott et al., 2015b, a; Abbott, 2019; Jeandel and Oelkers, 2015; Pearce et al., 2013; Arsouze et al., 2009;

50 Rempfer et al., 2011; Lacan and Jeandel, 2005b; Tachikawa et al., 2003; Johannesson and Burdige, 2007; Haley et al., 2017; Grenier et al., 2013). Removal of Nd from the water column occurs via sedimentation and complexation, and incorporation into authigenic ferromanganese oxides (Bayon et al., 2004; Du et al., 2016).

Relating to the inherent spatial heterogeneity in crustal ε_{Nd}, which is broadly governed by its age and composition, seawater

55 becomes 'tagged' with a unique ε_{Nd} signature derived from weathering of the proximal continents and hence tracks water mass provenance (Goldstein and Hemming, 2003; Robinson et al., 2021). Seawater ε_{Nd} is then redistributed throughout the ocean interior by advection and mixing, alongside particle cycling (see Tachikawa et al., 2017; van de Flierdt et al., 2016 for reviews). In the modern ocean, the ε_{Nd} signature of intermediate and abyssal waters display mostly conservative behaviour, co-varying with salinity in the Atlantic (Tachikawa et al., 2017; Goldstein and Hemming, 2003). The North Atlantic basin is

60 surrounded by old, unradiogenic continental cratons, yielding unradiogenic ε_{Nd} values for North Atlantic Deep Water (NADW) of around -13 (Lambelet et al., 2016). In contrast, the North Pacific seawater ε_{Nd} is more radiogenic with values between -4 and -2 (Amakawa et al., 2009; Fuhr et al., 2021; Behrens et al., 2018; Fröllje et al., 2016) due to proximate mantle derived volcanic material. Antarctic circumpolar waters have intermediate ε_{Nd} values of around -8.5 (Stichel et al.,

2012; Lambelet et al., 2018). These distinct water mass ε_{Nd} features form the basis for using the marine Nd cycle as a tool to
explore the global circulation. Furthermore, the ε_{Nd} of bottom water can be extracted from marine archives facilitating
palaeoceanographic investigations (e.g., Blaser et al., 2016; Martin and Scher, 2004; Piotrowski et al., 2004; Roberts et al.,
2010).

Intriguingly, in contrast to ε_{Nd} (i.e., the Nd paradox; Goldstein and Hemming, 2003), which is largely governed by water
mass mixing, dissolved Nd concentrations ($[Nd]_d$) deviate significantly from conservative behaviour (e.g., Zheng et al.,
2016), generally increasing linearly with depth and along the circulation pathway (i.e., with ventilation age) (van de Flierdt
et al., 2016). Internal vertical cycling via reversible scavenging is thought to play an important role in modulating the
distribution of Nd, where adsorption/incorporation and desorption/dissolution of Nd occurs on sinking and remineralising
particles throughout the water column (Siddall et al., 2008; Bacon and Anderson, 1982; Stichel et al., 2020). Alternatively, a
widespread benthic diffuse Nd flux was suggested to explain the Nd concentration and isotope decoupling (Haley et al.,
2017; Abbott et al., 2015b). However, observational data to confirm both processes are rare (e.g. Abbott, 2019; Abbott et al.,
2015b; Paffrath et al., 2021; Stichel et al., 2020), which limits a full quantification.

Moreover, whilst ε_{Nd} appears to trace large-scale ocean circulation features and water masses effectively, the specific
geochemical processes governing its distribution remain elusive (Abbott et al., 2019). Despite over four decades of research,
significant gaps in the understanding of the oceanic cycling of Nd persist, and mostly relate to quantifying the major input
pathways into, and subsequent internal cycling of Nd within the ocean (e.g., Haley et al., 2017; Tachikawa et al., 2017; van
de Flierdt et al., 2016; Abbott et al., 2021; Jeandel, 2016). For example, we are still missing a comprehensive estimate of a
particulate riverine flux as a major marine Nd source (Rousseau et al., 2015; Rahlf et al., 2021), constraints on reversible
scavenging processes and its efficiency throughout the water column (Siddall et al., 2008; Stichel et al., 2020; Paffrath et al.,
2021; Haley et al., 2021), and a quantification of the diffusive benthic flux to seawater (Abbott et al., 2015a). Furthermore,
the environmental conditions driving the extent and spatiotemporal variability of various elusive seafloor particle-seawater
interactions remain unknown (Tachikawa et al., 2017; Abbott et al., 2015a; Abbott, 2019; Abbott et al., 2016; Du et al.,
2016; Lagarde et al., 2020; Lacan and Jeandel, 2005b; Jeandel, 2016). The last point includes the absence of an established
quantification of both the spatial extent and the broad mobile sedimentary ε_{Nd} phases interacting with seawater or marine Nd
archives across the seabed, and specifically across remote and abyssal ocean regions (Robinson et al., 2021).

In an attempt to address such knowledge gaps, the international GEOTRACES programme has substantially increased
modern measurements of both seawater $[Nd]_d$ and ε_{Nd} (van de Flierdt et al., 2012; GEOTRACES Intermediate Data Product
Group, 2021), improving our understanding of the water column processes that govern marine Nd distributions (e.g., Basak
et al., 2015; Haley et al., 2021; Lambelet et al., 2018, 2016; Paffrath et al., 2021; Rahlf et al., 2020; Wang et al., 2021).
However, recent investigations and results from GEOTRACES have also alluded to some inconsistencies of localised highly

non-conservative behaviour, which challenge the simplified conservative assumptions of marine ε_{Nd} (Tachikawa et al., 2017;
Haley et al., 2017; Abbott et al., 2015b, 2019; Wang et al., 2021). Furthermore, due to the inherent challenges of directly
100 measuring fluxes that are both temporally and environmentally variable and globally widespread, there remain limited
process-based observations, which are necessary to both compliment the seawater measurements and capture fully the
marine geochemical cycling of Nd (Homoky et al., 2016).

Numerical models of the marine Nd cycle offer a unique means by which to constrain Nd budgets, providing quantitative
105 constraints on physical processes, and can be applied to investigate specific hypotheses regarding the mechanisms driving
seawater ε_{Nd} distributions (Tachikawa et al., 2003; Arsouze et al., 2009; Rempfer et al., 2011; Gu et al., 2019; Pöppelmeier et
al., 2020a, 2022; Pasquier et al., 2021; Siddall et al., 2008; Bertram and Elderfield, 1993; Arsouze et al., 2007; Rempfer et
al., 2012; Oka et al., 2021). As such, these models have formed a vital tool for improving the utility and interpretative
framework for ε_{Nd} as a modern and palaeoceanographic tracer.

110

Neodymium isotopes have been implemented into numerical models with a trend of ever increasing complexity, primarily in
terms of the type of model used, with a shift from fast and 'simple-to-use' box-models (Bertram and Elderfield, 1993;
Tachikawa et al., 2003) to full complexity ocean general circulation models (GCMs) (Arsouze et al., 2009; Rempfer et al.,
2011; Gu et al., 2019; Pöppelmeier et al., 2020a, 2022; Robinson et al., submitted). The latter of these model groupings has
115 the advantage of improved spatial resolution, ability to represent more physical processes and more dynamically consistent
ocean circulation fields (Flato et al., 2013), but at the cost of computational efficiency. Further complexity in numerical Nd
isotope schemes has been achieved in terms of increasingly detailed descriptions of marine Nd cycling, with preliminary
schemes representing ε_{Nd} in simple conservative mixing models applying crude surface boundary conditions (Bertram and
Elderfield, 1993; Tachikawa et al., 2003; van de Flierdt et al., 2004). The most recent Nd implementations in complex
120 models simulate both ^{143}Nd and ^{144}Nd isotopes individually, allowing for simultaneous representation of both [Nd]$_d$ and ε_{Nd}
and enabling a more detailed explicit representation of the major sources, sinks and cycling of marine ε_{Nd} and its sensitivity
to physical ocean circulation (Arsouze et al., 2009; Rempfer et al., 2011; Gu et al., 2019; Robinson et al., submitted).
Although these represent the most up-to-date knowledge of the marine Nd cycle, such models remain confounded by
inherent structural and parametric uncertainty, including uncertainty in either observation or process-based metrics,
125 alongside errors introduced within simplified representations of fundamental physics (i.e., 'parameterisations').

Full complexity Nd isotope enabled ocean models therefore rely on adjustable parameter values to capture the dominant
geochemical dynamics of a complex system, and we may optimise these inputs to find the model configuration that best
captures the observed process. The demand for higher computational power necessitated by the increasing sophistication and
130 complexity of Nd isotope schemes has meant only a handful of studies performed optimisation for their input parameters
within their relevant host ocean GCM models (e.g. in the ocean components of the Bern3D model; Pöppelmeier et al.,

2020b; Rempfer et al., 2011 and CESM1; Gu et al., 2019), especially since they require multi-millennial integrations to reach equilibrium. The schemes for which Nd cycling has been optimised faced a compounding problem for escalating computational demand by applying resource intensive systematic tuning (i.e., running over 100 simulations), using

135   suboptimal space filling design methodologies that may also lead to inefficient exploration of the input space. In addition, some of these models were restricted by previous assumptions regarding the dominating processes involved in the marine Nd cycle, which limited the development of appropriate model boundary conditions – notably here, an assumption that particle-seawater interaction is constrained to shallow continental margins (called into question by studies by Abbott et al., 2015b, a; Abbott, 2019; Haley et al., 2017).

140

In this study, we tackle these issues head-on, defining a new approach for efficiently refining a recent implementation of Nd isotopes in the ocean component of the Fast Met Office and UK universities Simulator (FAMOUS) GCM (Robinson et al., submitted). The scheme revisited and updated Nd sources, sinks and transformation of the tracer in line with increased observations and current findings relating to global marine Nd cycling (Blanchet, 2019; Robinson et al., 2021; Haley et al.,

145   2017; Siddall et al., 2008; Arsouze et al., 2009), and has been validated against global measurements of seawater $[Nd]_d$ and ε_{Nd} (Osborne et al., 2015, 2017; GEOTRACES Intermediate Data Product Group, 2021), substantiating that the major processes influencing the global marine Nd cycle are represented in the model. Here, we first assess and reduce the uncertainty within the input space of three key unconstrained parameters detailing major non-conservative processes within the global marine Nd cycle in a Bayesian framework (Sect. 2). We then present an optimised reference simulation (Sect. 3),

150   considered as 'best' from within the parameter space that satisfies physical reasoning in the context of what we know about Nd cycling, selected by minimising an objective loss function relating to model skill in reproducing modern measurements of both $[Nd]_d$ and ε_{Nd}. Subsequently, we undertake idealised sensitivity studies with this optimised reference simulation (Sect. 4), using a quasi-idealised experiment design to broadly investigate the preferential mobilisation of certain reactive sediment components under a seafloor-wide benthic flux model of marine Nd cycling. Finally, (Sect. 5), we investigate the

155   sensitivity of marine ε_{Nd} distributions between a margin-constrained versus a seafloor-wide benthic flux.

2 Methods

2.1 Model description

Neodymium isotopes (^{143}Nd and ^{144}Nd) have been fully implemented into the ocean component of the FAMOUS coupled atmosphere-ocean GCM (ND v1.0), representing three global sources of Nd to seawater: aeolian dust fluxes, riverine sources

160   and dissolution of marine sediment (i.e., benthic flux), and internal cycling and sedimentation processes via reversible scavenging (Robinson et al., submitted). The FAMOUS GCM (Smith et al., 2008; Jones et al., 2005; Smith, 2012; Jones et al., 2008) is derived from the Met Office's Hadley Centre Coupled Model V3 (HadCM3) AOGCM (Gordon et al., 2000). In brief, the atmospheric model of FAMOUS is based on quasi-hydrostatic primitive equations, has a horizontal resolution of 5° latitude

by 7.5° longitude, with 11 vertical levels on a hybrid sigma-pressure coordinate system, and a 1-hour timestep. The rigid-lid
165 ocean model has a horizontal resolution of 2.5° latitude by 3.75° longitude and 20 vertical levels, spaced unequally in thickness
from 10 m at the near-surface ocean to over 600 m at deep ocean depths, and a 12-hour timestep. The atmosphere and the
ocean are coupled once per day.

FAMOUS is currently capable of simulating on the order of 650 model years per wall clock day on 16 processors. As such, it
is well suited to running large ensembles (Gregoire et al., 2011) and performing sensitivity studies (Gregoire et al., 2015; Smith
170 and Gregory, 2009), alongside multi-millennial length simulations (Gregoire et al., 2012, 2015; Dentith et al., 2020), as is done
here.

We use the Met Office Surface Exchange Scheme (MOSES) version 1 (Cox et al., 1999; FAMOUS-MOSES1) generation of
the model. Although a more recent version of the land surface model does exist (MOSES2.2; Essery et al., 2003, 2001; Valdes
et al., 2017; Williams et al., 2013), when run for multi-millennia under constant pre-industrial boundary conditions the
175 published setup is known to produce a collapsed Atlantic Ocean convection accompanied by the formation of a strong deep
Pacific meridional overturning circulation (Dentith et al., 2019). Therefore, FAMOUS-MOSES1, which simulates more
realistic AMOC states over long (muti-millennia) integrations, is currently better optimised for exploring geochemical ocean
tracers. However, the Nd isotope scheme can be directly transferred to other versions of the UK Met Office Unified Model
(UM) version 4.5, including HadCM3/L or FAMOUS-MOSES2.2. A full description of the Nd isotope scheme in FAMOUS
180 is provided by Robinson et al. (submitted).

Dissolved seawater Nd in all our optimisation simulations (Sect. 2.2) is initialised from zero and integrated for 6,000 years
under the same constant pre-industrial boundary conditions as used by Robinson et al. (submitted); which, as determined in
our previous study, is sufficiently long for the Nd isotope scheme to adequately reach steady state under parameters within a
reasonable Nd inventory target response range (i.e., where global Nd inventory is 3.0×10^{12}–6.0×10^{12} g), whilst avoiding
185 unnecessary and costly additional run-time. Here, we define steady state as being when the Nd inventory becomes [near]
constant with time (i.e., < 0.0025 % change per 100 years). All the presented results refer to or show the centennial mean from
the end of the 6,000-year simulations.

2.2 Neodymium isotope scheme optimisation

To calibrate the Nd isotope scheme, we use an approach developed within the field of Bayesian Statistics, called History
190 Matching (Williamson et al., 2013). The framework uses a collection of tools to aid the quantification of uncertainty and rule
out combinations of model parameter values that produce unrealistic outputs. In calibrating the input space, history matching
does not require the assumption of probability distributions on the unknown model outputs; for this reason, it has seen
widespread uptake in the climate sciences where complex non-linear simulations make realistic judgements of output

probability distributions difficult. The approach consists of running an ensemble of simulations varying key input variables

195 simultaneously, via an efficient sampling method. The model output is then compared against observations using an implausibility metric to rule out unrealistic simulations. An emulator, a statistical regression (often a Gaussian Process: Rasmussen and Williams, 2006) relating model output (or metric) to input parameters, can be used to design good input combinations for running additional waves (i.e., ensembles) of simulations to further improve model performance. In this section, we describe our implementation of this approach, starting with our choice of tuning parameters (Sect. 2.2.1), then

200 introducing the Gaussian Process emulation, how we used previous sensitivity experiments to inform our new simulations, including our choice of target observations that informed the sampling of two waves of experiments (Sect. 2.2.2), and finally the metrics we used to identify the best simulations (Sect. 2.2.3).

2.2.1 Tuning parameters

To calibrate the Nd isotope scheme in the FAMOUS GCM, we explore the model input uncertainty of three key input variables:

205 (i) the reversible scavenging efficiency ($[Nd]_p/[Nd]_d$), which drives vertical cycling of marine Nd and represents the only Nd sink in the model; (ii) total sediment Nd flux (f_{sed}), which is especially important for governing Nd isotope distributions in the intermediate and deep ocean (Robinson et al., submitted); and (iii) riverine source scaling factor (α_{river}), which is a scaling applied to the surface riverine Nd source (Table 1). Note that the three tuning parameters ($[Nd]_p/[Nd]_d, f_{sed}$ and α_{river}) explored in this study do not vary spatially, and the total Nd sourced from aeolian dust is fixed for all the simulations. $[Nd]_p/[Nd]_d$ and

210 f_{sed} represent the major (and largely unconstrained) processes understood to govern $[Nd]_d$ and ε_{Nd} distributions (Rempfer et al., 2011; Gu et al., 2019; Siddall et al., 2008; Pöppelmeier et al., 2020a; Arsouze et al., 2009), and these two parameters are explored within both waves of analysis (Sect. 2.2.2). On the other hand, the decision to vary α_{river} in our optimisation is based on results presented by Rousseau et al. (2015), who found that in the Amazon Estuary, up to four times more Nd was supplied to the oceans via estuarine dissolution of river-sourced resuspended lithogenic material compared with dissolved sources. As

215 such α_{river} was used to examine, to a first order, enhanced Nd sourced at river mouths, and this parameter was explored during the second wave of analysis (Sect. 2.2.2).

Table 1: Parameters chosen for the optimisation of the Nd isotope scheme in FAMOUS and their initial ranges. References are provided for the choice of initial range.

Parameter	Initial range	Unit	Description	References
$[Nd]_p/[Nd]_d$	$[0.001, 0.006]$	-	Reversible scavenging efficiency	(Robinson et al., submitted)
f_{sed}	$[1.5 \times 10^9, 6.0 \times 10^9]$	$g(Nd) \, yr^{-1}$	Total seafloor sediment flux	(Robinson et al., submitted)

| α_{river} | [1.0, 4.0] | - | Riverine source scaling | (Rousseau et al., 2015) |

220

The objective of our tuning was to statistically optimise these three key model input variables within the FAMOUS Nd isotope scheme, aiming to reduce parametric uncertainty and substantially refine the plausible parameter space to improve the model's skill at representing both modern $[Nd]_d$ and ε_{Nd} distributions. Despite FAMOUS being a fast GCM, running a simulation to equilibrium still requires 10 days on 16 processors. To make best use of computing resources, we therefore adopted an approach

225 that uses an efficient sampling strategy; Gaussian Process emulation to 'guess' optimal parameter value combinations and multiple waves of experiments to progressively refine the model calibration.

2.2.2 Statistical design of multi-wave ensemble

Gaussian Process (GP) emulators are non-parametric statistical regression models that flexibly represent chosen model output or performance metrics as a function of a subset of input parameters, together with an uncertainty on that prediction

230 (Rasmussen and Williams, 2006; Astfalck et al., 2019). We describe the model output y as a function of a vector of input parameters θ expressed as:

$$y(\theta) \, GP\big(m(\theta), k(\theta, \theta')\big), \tag{1}$$

where m represents a mean function used to provide parametric prior model beliefs, and k represents a covariance function. Our input space, θ, is defined by the uncertain Nd scheme parameters: $[Nd]_p/[Nd]_d$, f_{sed}, and α_{river} (see section above). The

235 effects of parameters not explicitly represented in θ are handled by the random stochasticity embedded in the covariance function.

Building such a *GP* emulator to predict the plausible input parameter regions first requires results from multiple simulations with the Nd isotope scheme, forming a reference exploratory ensemble. Here, for efficiency, we used output of annual global

240 Nd inventories ($Nd(I)$) and residence times (τ_{Nd}) from 11 existing single parameter perturbation simulations, which formed part of the preliminary sensitivity analysis of the new Nd isotope scheme performed by Robinson et al. (submitted; Fig.1 triangles), including two additional experiments run under a combined high $[Nd]_p/[Nd]_d$ and f_{sed}, with α_{river} set to 1.0 in one simulation, and set to 3.0 in the other (see Supplementary Table S1 for the specific combination of parameter values used in each simulation, simulation names are denoted by their unique five-letter Met Office Unified Model identifier). We refer to

245 these simulations as the "training set".

We chose to focus the initial optimisation of the Nd isotope scheme on model outputs of annual global Nd inventories ($Nd(I)$) and residence times (τ_{Nd}) as these relatively simple and hence easy to handle terms encompass the balance of all Nd sources and sinks in the model. Further, $Nd(I)$ and τ_{Nd} determine model equilibrium and the lifetime of Nd in the ocean, the latter of

250   which drives the distinct basinal ε_{Nd} signals that are fundamental to the water mass tracer properties of marine ε_{Nd}. Additionally, and for each wave of the multi-wave ensemble, we set a target range for $Nd(I)$ and τ_{Nd} (Table 2). The choice of target bounds for $Nd(I)$ (Table 2) reflect the widely recognised estimated global $Nd(I)$ of 4.2×10^{12} g (Tachikawa et al., 2003). Alongside these target $Nd(I)$ bounds, specific for sampling in Wave 2, we employ a maximum threshold residence time of Nd (i.e., $\tau_{Nd} <$ 1,000 years). This value was chosen based on results from Robinson et al. (submitted) who demonstrated where Nd ocean

255   residence times are over 1,000 years, close to the timescales of global overturning circulation, simulated Nd becomes well mixed in the ocean which acts to globally homogenise the ε_{Nd} signal.

Table 2: Design of the multi-wave FAMOUS Nd isotope scheme optimisation ensemble. Previous simulations from Robinson et al. (submitted) used as the *GP* 'training set' are not shown here.

	Number of simulations	Parameters explored	$Nd(I)$ target range ($\times 10^{12}$ g)	τ_{Nd} target range (years)
Wave 1	8	$[Nd]_p/[Nd]_d$, f_{sed}	[3.0, 5.0]	NA
Wave 2	15	$[Nd]_p/[Nd]_d$, f_{sed}, α_{river}	[3.7, 4.7]	[< 1,000]

260

The *Gaussian Process emulator* was fitted to the "training set" of simulations to emulate the predictive mean $Nd(I)$ and τ_{Nd}, as a function of the uncertain parameters $[Nd]_p/[Nd]_d$, f_{sed}, and α_{river}. From these results, we predict the plausible region of the parameter space, called not-ruled-out-yet (NROY) space, as all the combinations of parameter values that would likely produce $Nd(I)$ and τ_{Nd} within their target ranges (Table 2), given the uncertainty in the *GP* emulator. We successively refine this region

265   by running two waves of ensembles. Mathematically, this can be described as follows. Using the *GP* emulators, at any unexplored location, θ, we obtain prediction of $y(\theta)$ described by an expectation $E[y(\theta)]$ and variance $var[y(\theta)]$. Appealing to a common heuristic (here, Chebyshev's inequality) we describe the prediction interval of $y(\theta)$, as $P(\theta) = \left[E[y(\theta)] - 3\sqrt{var[y(\theta)]}, E[y(\theta)] + 3\sqrt{var[y(\theta)]}\right]$ so that $y(\theta) \in P(\theta)$ with high probability. This is a conservative rule of thumb that considers all the emulated values within 3 standard deviations of the mean (Chebyshev, 1867).

270   For each wave we apply the set of target ranges for $Nd(I)$ and τ_{Nd} (documented in Table 2). We define the NROY space as the collection of input parameters, θ^{NROY}, whose prediction intervals $P(\theta^{NROY})$ contain values of $Nd(I)$ and τ_{Nd} within their specified target ranges. Define the target ranges by T, mathematically we describe the NROY space as:

$$NROY = \{\theta : P(\theta) \cap T \neq \{0\}\},\tag{2}$$

that is, the values of θ where the intersection of $P(\theta)$ and T are not the null set {0}. In plain language, this means that we

275   define the *NROY* space as all the parameter combinations for which the emulator predicts it is plausible that results will be within our target range.

Combinations of parameter values for each wave (Fig. 1) are sampled using k-extended Latin Hypercube sampling (Williamson, 2015) within the *NROY* space so that design locations are optimally spaced with respect to the target values

280   (Table 2).
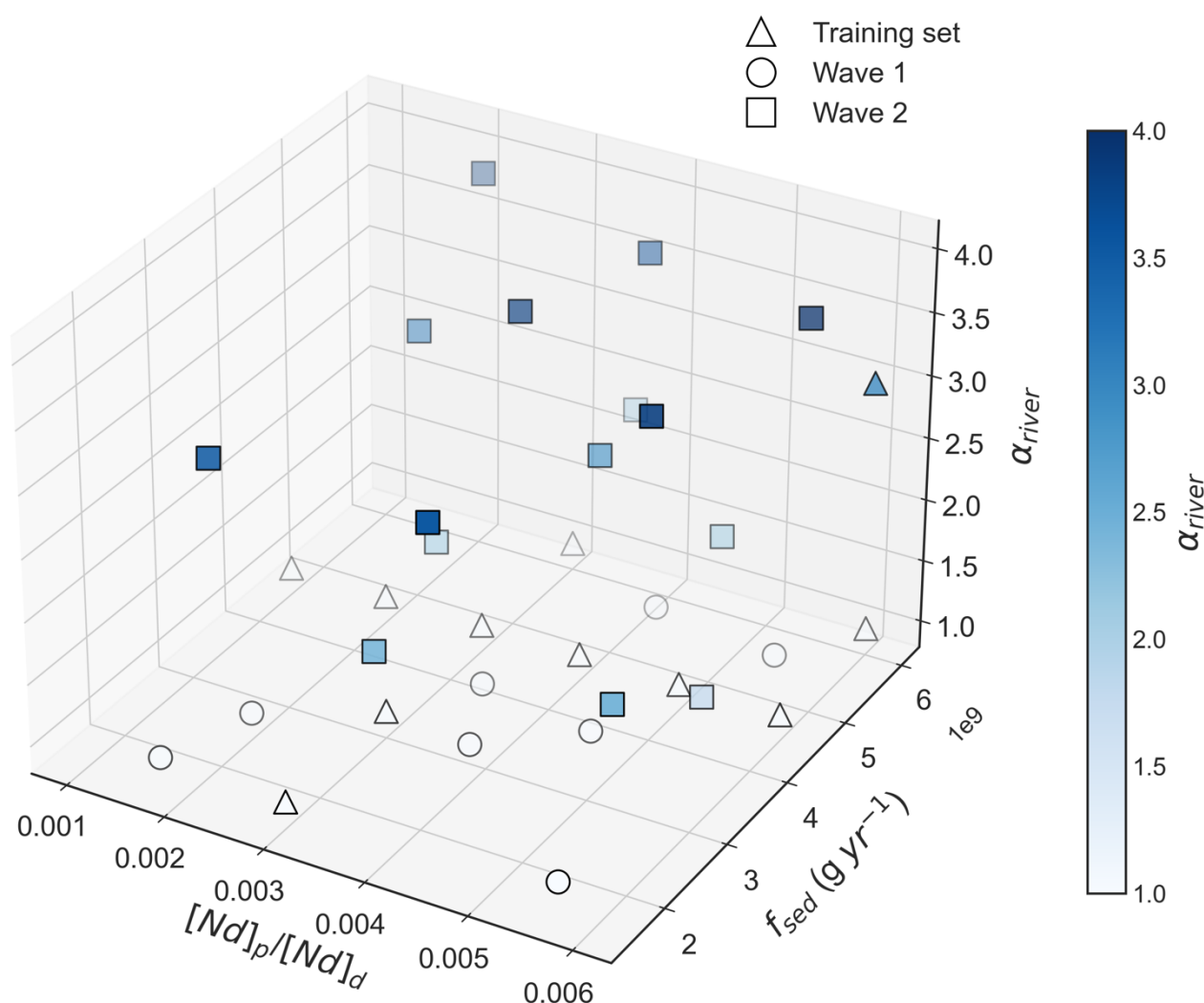
Figure 1: Parameter combinations of $[Nd]_p/[Nd]_d$ (x-axis), f_{sed} (y-axis) and α_{river} (z-axis and colour of filled markers) in the multi-wave FAMOUS Nd isotope scheme optimisation. Triangles indicate simulations in the training set, circles are for simulations in Wave 1, and squares are for simulations in Wave 2.

285   In Wave 1, we vary the two parameters detailing the major non-conservative processes believed to govern marine Nd cycling

($[Nd]_p/[Nd]_d$ and f_{sed}). Wave 2 further includes the additional third tuneable parameter (α_{river}), thus, to ensure the regions of

plausible parameter space adequately capture this additional dimension, we increase the number of simulations in Wave 2 to 15 (Table 2).

290   We sample the eight simulations in Wave 1 such that *GP* predictive mean $Nd(I)$ is between 3.0×10^{12} g and 5.0×10^{12} g, which are intentionally wide bounds designed to better encompass the largely unexplored *NROY* parameter space and associated uncertainty arising from the limited (11) simulations forming the exploratory ensemble. We do not yet constrain τ_{Nd}.

The *GP* emulator is updated for Wave 2, based on the additional results of Wave 1, to reassess the uncertainty in the remaining
295   plausible input space. The additional information gained from Wave 1 reduces uncertainty and improves the predictive capability of the *GP*. This enables us to apply refined bounds on the mean $Nd(I)$ that are closer to the global $Nd(I)$ target reference of 4.2×10^{12} g ($\pm 0.5 \times 10^{12}$ g), and to introduce the τ_{Nd} target (Table 2). Using the results of the Wave 2 simulations, we describe the final *NROY* space by the Wave 2 criteria with the *GP* emulator trained on all resulting data from the training Wave 1 and Wave 2 simulations. After two waves of simulations, the maximum predictive standard deviations of $Nd(I)$ and
300   τ_{Nd} within the NROY space is 0.22×10^{12} g and 46 years, respectively; we deem this to be a sufficient reduction in parametric uncertainty to end the iterative process of performing further model ensembles to inform the *GP*. More resources could have been allocated to further reduce the uncertainty, but with diminishing benefits. Thus, with only 23 new simulations (instead of the 100+ used in previous studies; Rempfer et al., 2011; Gu et al., 2019; Pöppelmeier et al., 2020a), we are in a position to optimally calibrate the Nd scheme.

305   **2.2.3. Identifying the best performing simulation**

Following the multi-wave parameter analysis of the FAMOUS Nd isotope scheme, we apply an updated *GP* emulator to determine the parameter combinations within our remaining plausible input space to produce a statistically optimised reference simulation (named '*REF*') that best matches modern measurements of $[Nd]_d$ and ε_{Nd}. We first determine model skill by returning the mean absolute error (MAE):

310

$$MAE = \frac{1}{N} \sum_{k=1}^{N} |obs_k - sim_k|, \tag{3}$$

where obs_k and sim_k are measured and simulated $[Nd]_d$ or ε_{Nd} respectively, and k is an index over all observational data. For each measurement – based on its longitude, latitude, and depth – the value predicted by the simulation is extracted and the mean deviation of simulated and observed $[Nd]_d$ and ε_{Nd} is presented in pmol kg^{-1} and ε_{Nd}-units respectively. Here we chose
315   specifically not to apply a grid box volume weighting to the MAE, which would act to emphasise abyssal Pacific results in our assessment of model skill (due to the large area of the abyssal Pacific Ocean), where there are few observations and relatively low variability in Nd distributions. The advantage of using an unweighted MAE is that the assessment metric better scrutinises regions with larger (spatial) gradients in both $[Nd]_d$ or $\varepsilon_{Nd;}$ i.e., at the surface and high latitudes. However, we acknowledge

neither the horizontal nor vertical distribution of global seawater $[Nd]_d$ or ε_{Nd} observational data are even (Robinson et al.,
320 submitted), and some local surface features captured in the seawater measurements will not be represented in FAMOUS due
to model resolution, introducing some bias into the cost function. The measurements used in this assessment are from the
seawater REE compilation used by Osborne et al (2017, 2015), augmented with more recent measurements including data
from the GEOTRACES Intermediate Data Product 2021 (GEOTRACES Intermediate Data Product Group, 2021; sections
GA02, GA08, GP12, GN02, GN03, GIPY05). Combined, the utilised observational database represents a total of 6,048 $[Nd]_d$
325 and 3,278 ε_{Nd} measurements. Notably, we omit measurements of $[Nd]_d > 100$ pmol kg^{-1} from the model data comparison here
because these represent very localised signals, which we do not attempt to resolve (Robinson et al., submitted). In some
instances, near land grid cells, the location of the measured and modelled Nd being compared may not match. In such cases,
we employ a nearest neighbour algorithm to extract the modelled value from the closest ocean model grid cell. Furthermore,
if multiple measurements occur within one model grid cell, the arithmetic mean of the values is used for our comparison to
330 model results, and as such, $n = 3,471$ and $2,136$ for the calculation of both $MAE_{[Nd]}$ and $MAE_{\varepsilon Nd}$ respectively.

We then standardise the mean absolute errors (MAE = J_i) for both $[Nd]_d$ and ε_{Nd} (where $i = [Nd]_d$ and ε_{Nd}) as:

$$STD\_J_i = (J_i - E(J_i))/Sd(J_i), \qquad\qquad (4)$$

where E(.) and Sd(.) represent the empirical mean and standard deviation. We then define our loss function (J_{loss}) as:

$$J_{loss} = STD_{J_{[Nd]}} + STD_{J_{\varepsilon Nd}}, \qquad\qquad (5)$$

335 which we minimise over the NROY space. The minimisation constraints applied to sample the *REF* parameters for $Nd(I)$ and
τ_{Nd} (i.e., the bounds within which we minimise for J_{loss}) are consistent with those imposed during Wave 2 of the multi-wave
parameter exploration (Table 2). These constraints are what we define as the capability of the model to satisfy physical
reasoning within its simulation of the marine Nd cycle, alongside an additional constraint regarding an upper limit of the
reversible scavenging efficiency ($[Nd]_p/[Nd]_d < 0.0045$). This maximum threshold for $[Nd]_p/[Nd]_d$ was set following results
340 from the multi-wave analysis demonstrating that notwithstanding improved $J_{\varepsilon Nd}$, above this threshold and particularly in the
Pacific, numerical instabilities in simulated ε_{Nd} occur within the surface layers due to near-zero $[Nd]_d$ resulting from an over-
strong particle scavenging.

Our optimisation procedure and specific choice of physical ($Nd(I)$ and τ_{Nd}; Table 2) and parameter ($[Nd]_p/[Nd]_d < 0.0045$)
345 bounds are somewhat arbitrary, yet, as detailed in Sect 2.2.2, we approximate these from prior knowledge of marine Nd cycling
and our most up-to-date capabilities in choosing appropriate constraints to solve for J_{loss} that improve model skill in
representing the modern marine Nd cycle (Rempfer et al., 2011; Arsouze et al., 2009; Siddall et al., 2008; Tachikawa et al.,
2003). To test the sensitivity of simulated Nd distributions to the choice (or prioritisation) of target summary metrics (and thus
what combinations of f_{sed}, $[Nd]_p/[Nd]_d$ and α_{river} are identified as optimal), we ran two additional simulations alongside *REF*.

350   These use parameter value combinations that the *GP* emulator predicts will minimise $J_{[Nd]}$ (simulation *REF_CONC1*) and $J_{\varepsilon Nd}$ (simulation *REF_IC*), removing the minimisation constraints applied for $Nd(I)$ and $\tau_{Nd,}$ hence prioritising performance for $[Nd]_d$ and ε_{Nd} respectively, rather than balancing the standardised performance for both.

3 Optimisation results and discussion

3.1 Overview of multi-wave ensemble and parameter influence

355   The multi-wave ensemble explored the response of simulated $[Nd]_d$ and ε_{Nd} in the FAMOUS GCM to effective space-filling variations within the NROY parameter space for the three tuning parameters: $[Nd]_p/[Nd]_d, f_{sed}$ and α_{river}. Neodymium inventory in all experiments in the ensemble increases considerably within the first 1,000 years of simulation, and by the end of the simulations, the majority reach steady state under a range of different $Nd(I)$ (Fig. 2). There is less variance in the simulated $Nd(I)$ from the simulations in Wave 1. This is as expected since the first wave only explored the two-dimensional input space

360   of $[Nd]_p/[Nd]_d$ and f_{sed}, which were the focus of the systematic exploration within our previous sensitivity analysis (Robinson et al., submitted). As such, after Wave 1, the *GP* benefited from a greater exploration of the 2D parameter space, and thus from additional constraints on regions of the space that are unfeasible/unphysical, herby increasing the *GP*'s predictive power. By adding the river scaling (α_{river}) parameter in Wave 2, we introduced an additional and widely unexplored degree of freedom into the simulations, producing a greater range of simulated $Nd(I)$ (Fig. 2).

365
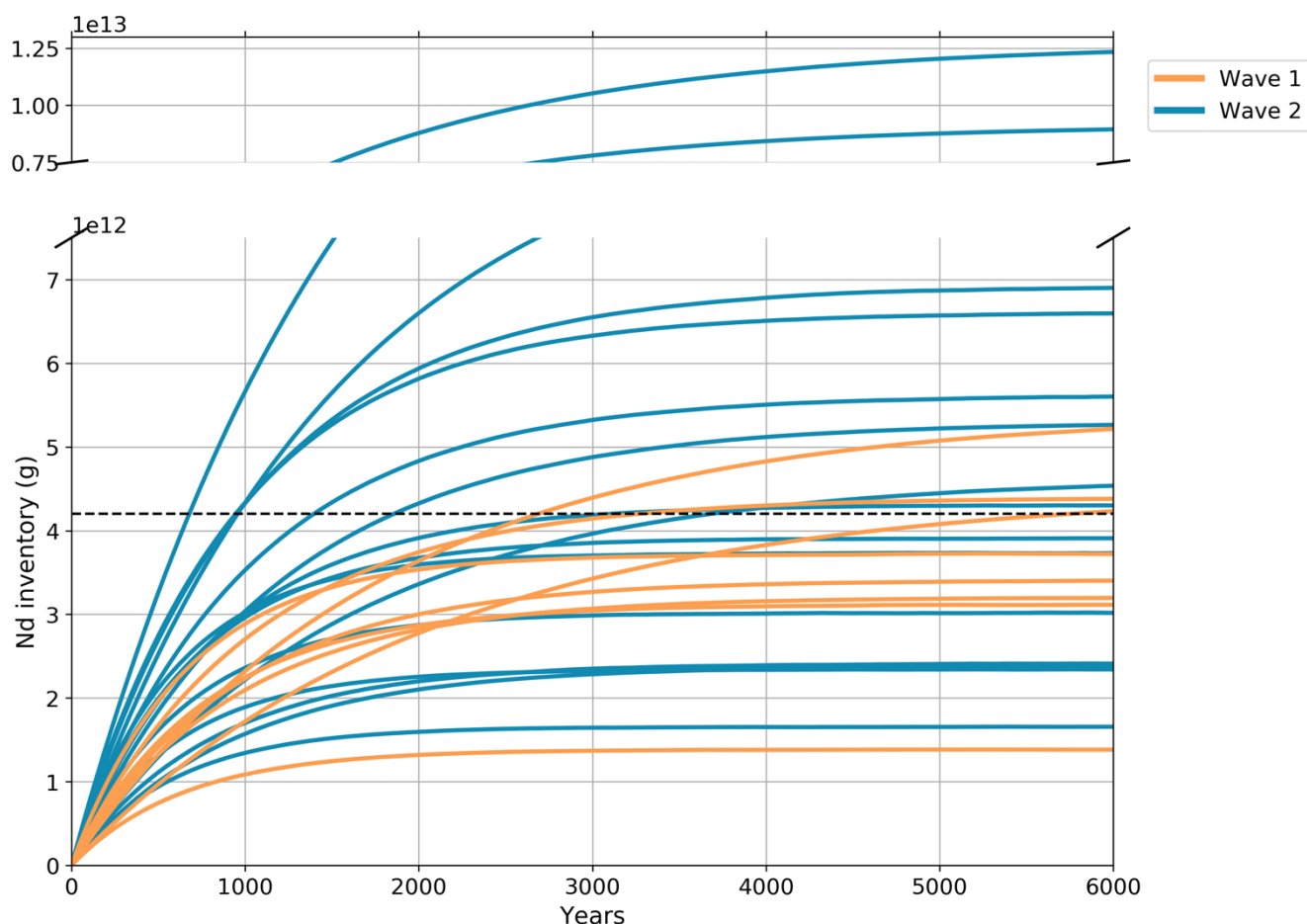
Figure 2: Timeseries of simulated global Nd inventory (g) from the multi-wave parameter tuning ensemble. Orange and blue lines are from simulations in Wave 1 and 2 respectively, and the dashed line represents the estimated global marine Nd inventory of 4.2×10^{12} g from Tachikawa et al. (2003).

370

The lowest simulated $Nd(I)$ of 1.38×10^{12} g occurs within Wave 1; this simulation (*XPGTG*; Supplementary Table S1) has a strong particle scavenging efficiency ($[Nd]_p/[Nd]_d = 0.0056$) combined with a low sediment source ($f_{sed}=1.59 \times 10^9$ g yr^{-1}), and no riverine source scaling to account for dissolution of river particulates (i.e., $\alpha_{river} = 1.0$). The low collective total Nd source (f_{total}) to the ocean of 2.36×10^9 g yr^{-1} combined with a parameterisation of strong sinking and removal in the model causes Nd

375 to rapidly (within 3,000 years) reach equilibrium under low $Nd(I)$. In contrast, the Nd sources and sinks within two simulations from Wave 2 (*XPHJH* and *XPHJI*: Supplementary Table S1) are especially unbalanced (i.e., Nd input outweighs Nd removal). Here the parameter combinations result in unrealistically large $Nd(I)$, ranging from 8.95×10^{12} g up to 12.3×10^{12} g, which is still increasing considerably at the end of the simulation. Importantly, though, both of these high $Nd(I)$ simulations explore similar regions of the parameter space, with combinations of low reversible scavenging efficiencies (where $[Nd]_p/[Nd]_d \leq$

380 0.0023) and high Nd sources ($f_{\text{total}} \geq 6.32 \times 10^9$ g yr^{-1}). A few simulations with reasonable $Nd(I)$, but which have not reached steady state, all share low reversible scavenging efficiencies relative to their total Nd source magnitudes. Here, we have learned important information from the GP, and all such simulations are determined to be within the regions of the refined parameter space that are now ruled out; based on what we deem to be an unphysical Nd residence time that is too similar to or longer than the typical timeframe of global deep ocean overturning (Sect. 2.2.2.).

385

The relationship between the three tuning parameters and their controls on determining $Nd(I)$ and τ_{Nd} demonstrate foremost that $[Nd]_p/[Nd]_d$, f_{sed} and α_{river} are almost equally important in determining the variation in $Nd(I)$, this is because each parameter governs major seawater Nd source/removal (Fig. 3). Alternatively, τ_{Nd} also shows a very strong correlation between varying $[Nd]_p/[Nd]_d$, which is unsurprising considering $[Nd]_p/[Nd]_d$ drives the only sink in the model, but clearly demonstrates the

390 important role of scavenging intensity for governing simulated Nd residence time in the ocean. In contrast, the lack of correlation between f_{sed} and α_{river} reduces direct impact of these parameters on τ_{Nd}.
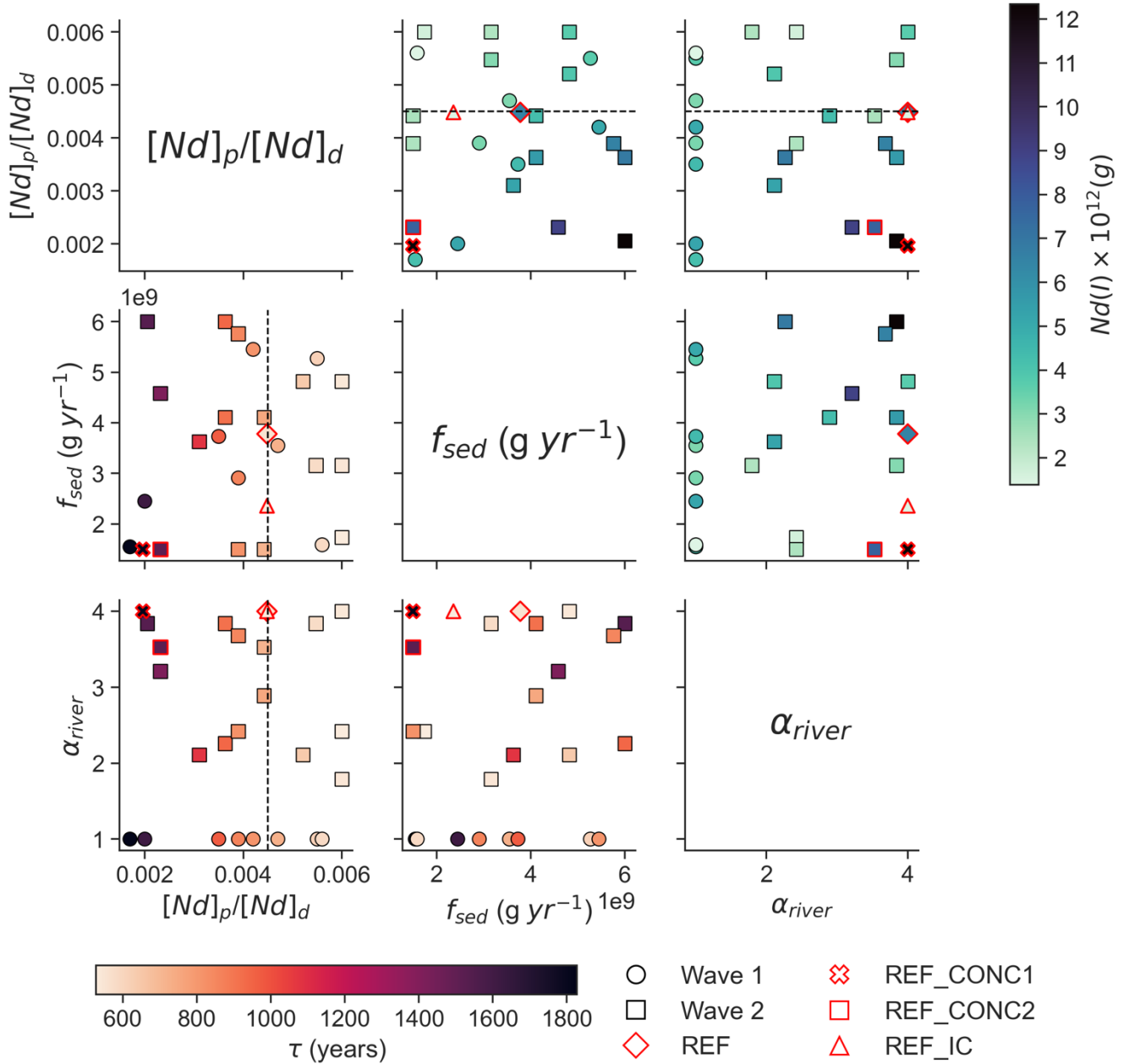
Figure 3: Simulated Nd inventory ($Nd(I)$) and residence time (τ_{Nd}) from *GP* predicted parameter combinations in the multi-wave FAMOUS Nd isotope ensemble and optimisation. Circles and squares represent the parameter combinations in Wave 1 and 2 respectively. Output from *REF* (red diamond), *REF_CONC1* (red cross), *REF_CONC2* (red square, see Table 3), and *REF_IC* (red triangle) simulations are overlain. The dashed black line indicates the upper limit of the reversible scavenging efficiency ($[Nd]_p/[Nd]_d$ < 0.0045; Sect. 2.2.3) imposed for identifying the best performing simulations (i.e., *REF, REF_CONC1 and REF_IC*) to avoid numerical instabilities in the surface layers resulting from too strong particle scavenging.

There is a complex relationship between the three tuning parameters and their controls on model skill in simulating $[Nd]_d$ (determined by the MAE, $J_{[Nd]}$; Fig. 4). Broadly, best $[Nd]_d$ model-data fit occurs under balanced parameter combinations of

400   low scavenging intensity ($[Nd]_p/[Nd]_d$) and low Nd source magnitudes (i.e., low combined f_{sed} and α_{river}) moving to high scavenging balanced by high Nd source magnitudes. Conversely, worst $[Nd]_d$ model-data fit occurs under low scavenging intensity coupled with high source magnitudes, mostly due to imbalanced Nd budgets causing unrealistically high $[Nd]_d$ accumulation in the ocean. The largest variance in $J_{[Nd]}$ exist under different f_{sed} and α_{river} when under low particle scavenging ($[Nd]_p/[Nd]_d < 0.003$), indicating that within this region of parameter space, $[Nd]_p/[Nd]_d$ impacts are minor and the two source

405   parameters exert a bigger influence on $[Nd]_d$ (Fig. 4). On the other hand, there is a much clearer relationship between the tuning parameters and $J_{\varepsilon Nd}$, with minimised $J_{\varepsilon Nd}$ for larger $[Nd]_p/[Nd]_d$. Reversible scavenging efficiency therefore explains most of the variance regarding model skill in simulating ε_{Nd} in our ensemble, mostly due to strong vertical cycling keeping τ_{Nd} below the global overturning time and enhancing localised basinal ε_{Nd} signals. More indistinguishable patterns for f_{sed} and α_{river} suggest these parameters are less influential for minimising $J_{\varepsilon Nd}$.

410
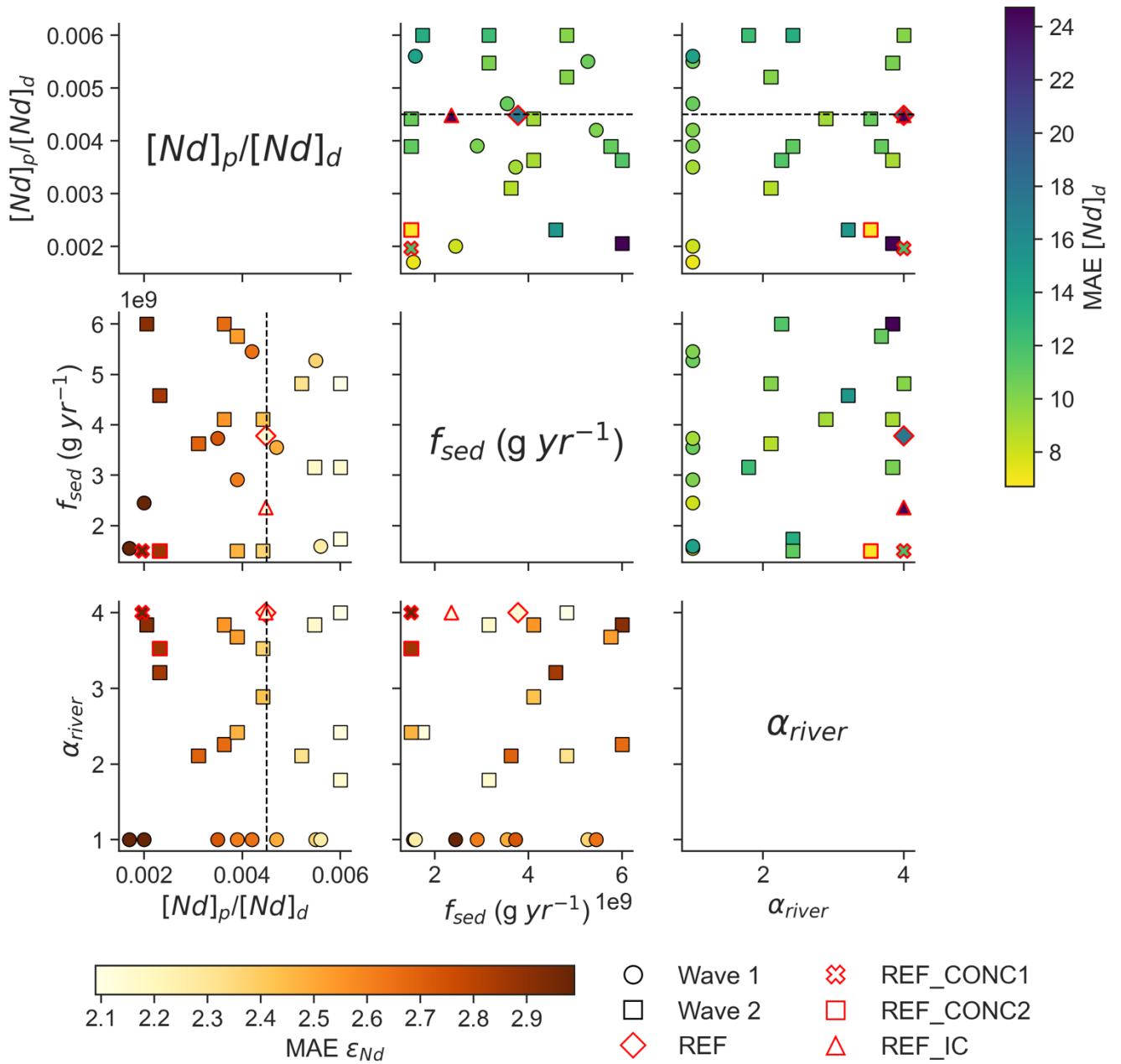
Figure 4: Mean absolute error (MAE$_i$: J_i, Eq. (3)) values indicating model skill in representing modern measurements of $[Nd]_d$ ($J_{[Nd]}$) and ε$_{Nd}$ ($J_{\varepsilon Nd}$) from *GP* predicted parameter combinations in the multi-wave FAMOUS Nd isotope ensemble and optimisation. Circles and squares represent the parameter combinations in Wave 1 and 2 respectively. Output from *REF* (red diamond), *REF_CONC1* (red cross), *REF_CONC2* (red square, see Table 3), and *REF_IC* (red triangle) are overlain. The dashed black line indicates the
415 **upper limit of the reversible scavenging efficiency ($[Nd]_p/[Nd]_d < 0.0045$; Sect. 2.2.3) imposed for identifying the best performing simulations (i.e., *REF, REF_CONC1 and REF_IC*) to avoid numerical instabilities in the surface layers resulting from an over strong particle scavenging.**

3.2 Optimised reference simulation

Our statistically optimised reference simulation (*REF*) embodies our current 'best' estimate of the combination of parameter
420 values that represent the modern marine Nd cycle in FAMOUS, based upon minimising the expected loss function (J_{loss}: a standardised MAE of both $[Nd]_d$ and ε_{Nd}, from Eq. (5)). We highlight, here, that our estimate necessitates subjective decisions including our choice of loss function (J_{loss}), choice of tuneable parameters (Sect. 2.2.1), physical targets from which to minimise J_{loss} within (i.e., mean $Nd(I)$ of 4.2×10^{12} g ($\pm 0.5 \times 10^{12}$ g), $\tau_{Nd} < 1,000$ years; Sect. 2.2.2), and an upper limit on the reversible scavenging efficiency to prevent numerical instabilities in the surface layers (i.e., $[Nd]_p/[Nd]_d < 0.0045$; Sect. 2.2.3), combined
425 with the intrinsic parametric and structural uncertainty typical within GCMs like FAMOUS. As such, it is unlikely that a single 'best' configuration exists. Rather, a subset of different parameter values within the refined parameter space (Sect. 3.1) could yield multiple optimal solutions, though we recognise other subsets would capture similar key characteristics of the modern marine Nd cycle as our selection of values for *REF*.

430 The $Nd(I)$ in *REF* is 4.27×10^{12} g and has reached steady state (where rate of change in final 100 years is 0.0012%), and thus is in excellent agreement with previous Nd isotope enabled model inventories (Tachikawa et al., 2003; Rempfer et al., 2011; Gu et al., 2019; Arsouze et al., 2009). The total Nd source to the ocean (f_{total}) is 5.9×10^9 g(Nd) yr^{-1}, sitting within the range of recent estimates of 4.5×10^9 to 6.1×10^9 g(Nd) yr^{-1} (Rempfer et al., 2011; Gu et al., 2019), and Nd residence time (τ_{Nd}) is 727 years (where $\tau_{Nd} = Nd(I)/f_{total}$), which is also inside the range estimated by recent isotope enabled models (690-785 years;
435 Rempfer et al., 2011; Gu et al., 2019; Pöppelmeier et al., 2020a). A full list of final optimised parameter values for *REF* are presented in Supplementary Table S2. Moreover, the optimised scheme apportions the magnitude of simulated Nd sources to seawater: the sediment source via a seafloor wide benthic flux represents the largest Nd source contributing 64% of the total Nd source, riverine sourced Nd contributes 30%, whilst dust sources make up the final 6%. Our partition of Nd sources are most comparable to recent estimates by Pöppelmeier et al. (2020) (where sediment contributed 60%, rivers 32% and dust 9%),
440 likely related to the river scaling applied in both studies. Moreover, the spatially uniform seafloor-wide benthic flux of 3.78×10^9 g(Nd) yr^{-1} (i.e., f_{sed}) corresponds to a sediment flux (per area) of 2.96 pmol cm^2 yr^{-1}. This value is similar to the few existing measurements of a benthic Nd flux across diverse sedimentary environments, which are mostly on the order of 10 pmol cm^2 yr^{-1} (Abbott, 2019; Abbott et al., 2015a; Du et al., 2018; Haley et al., 2004). Compared with model estimates of the sediment flux, our value is close to the global benthic flux estimated by Pöppelmeier et al. (2020) of 5.4 pmol cm^2 yr^{-1}, and lower than
445 the value of 20-30 pmol cm^2 yr^{-1} estimated by Du et al. (2020).

For comparison, we chose to run two additional simulations where the *GP* predicted parameter values to minimise for $[Nd]_d$ (i.e., $J_{[Nd]}$) or for ε_{Nd} (i.e., $J_{\varepsilon Nd}$), named *REF_CONC1* and *REF_IC* respectively (Table 3). Interestingly, one simulation from Wave 2 of the multi-wave ensemble (*XPHJF*) performs better for reproducing global measurements of $[Nd]_d$ than the
450 simulation predicted by the GP emulator to minimise $J_{[Nd]}$ (REF_CONC1). This is demonstrated by the lower MAE ($J_{[Nd]}$) of

6.69 pmol kg^{-1} compared to 7.51 pmol kg^{-1} in *REF_CONC1*; for subsequent discussion and in the figures, we name this simulation *REF_CONC2*. The reason that *REF_CONC1* performed slightly worse than *REF_CONC2* in terms of $[Nd]_d$ performance can be attributed to imprecision in the *GP*. This emulator uncertainty arises from the inability to run the simulator through every possible input configuration as a result of limited computing resources, resulting in a degree of statistical error

455 surrounding the prediction of optimised parameters (Rasmussen and Williams, 2006; Kennedy and O'Hagan, 2001). Furthermore, uncertainties introduced into the *GP* due to inaccuracies within the observational measurements (e.g., Pahnke et al., 2012) adds an additional degree of uncertainty to the prediction. However, the similar input values for *REF_CONC1* and *REF_CONC2* – whereby the main difference is from the smaller α_{river} of 3.53 in *REF_CONC2* compared to 4.0 in *REF_CONC1*, resulting in a smaller total Nd source to seawater (i.e., f_{total}) – demonstrates the multi-wave exploration (Sect.

460 3.1) sufficiently explored the parameter space. This illustrates that the *GP* effectively refines plausible regions of the input space for optimising model performance, albeit with an associated uncertainty in the prediction.

Table 3: Overview of the parameter values and general model skill for the optimised *REF* simulation, which the *GP* minimised for J_{loss} (Eq. (5)) compared to simulations which the *GP* minimised for $J_{[Nd]}$ (*REF_CONC1*) and $J_{\varepsilon Nd}$ (*REF_IC*) separately. Due to
465 **uncertainty associated with the *GP* prediction, *REF_CONC2* describes a simulation from Wave 2 of the multi-wave parameter analysis (XPHJF) which performed best in terms of minimising for $J_{[Nd]}$.**

Simulation name	UM identifier	f_{sed} ($\times10^9$ g yr^{-1})	$[Nd]_p/[Nd]_d$	α_{river}	f_{total} ($\times10^9$ g yr^{-1})	$Nd(I)$ ($\times10^{12}$ g)	τ_{Nd} (yrs)	$J_{[Nd]}$ (n=3471)	% within 10 (pmol kg^{-1})	$J_{\varepsilon Nd}$ (n=2136)	% within 3 ε_{Nd}-units
REF	*XPIAB*	3.78	0.00448	4.0	5.87	4.27	727	8.83	68	2.37	67
REF_CONC1	*XPIAD*	1.5	0.00196	4.0	3.59	5.51	1534	7.51	73	2.84	63
REF_CONC2	*XPHJF*	1.5	0.0023	3.53	3.38	4.54	1341	6.69	81	2.77	63
REF_IC	*XPIAC*	2.36	0.00448	4.0	4.45	3.16	711	9.42	63	2.34	68

The optimised parameter values vary between the three experiments that minimise J_{loss} (*REF*), $J_{[Nd]}$ (*REF_CONC2*), and $J_{\varepsilon Nd}$ (*REF_IC*). Notably, *REF* has the highest sediment source (f_{sed}), and both *REF* and *REF_IC* have the highest scavenging
470 efficiency $[Nd]_p/[Nd]_d$ of 0.00448, which lies close to the imposed upper limit on the reversible scavenging efficiency (i.e., $[Nd]_p/[Nd]_d < 0.0045$) (Table 3). This demonstrates that, in our ensemble, efficient reversible scavenging is key for determining ε_{Nd}. Whereas the much lower $[Nd]_p/[Nd]_d$ of 0.0023 in *REF_CONC2* facilitates a longer marine Nd residence time due to less scavenging and removal via sedimentation, which allows Nd isotopes to become better mixed throughout the ocean, improving

model representation of $[Nd]_d$, but at the expense of removing distinct inter-basin water mass ε_{Nd} signals (Robinson et al.,
475   submitted).

Riverine source scaling, to account for dissolution of river particulates, in all optimised simulations (*REF*, *REF_CONC2*, and
REF_IC) is set to the upper bound of the scaling parameter range considered (where α_{river} is set to, or close to 4.0; Table 3).
Here, indicating that an enhanced Nd flux from rivers considerably favours model performance for both $[Nd]_d$ and ε_{Nd}. This
480   may suggest a particulate river source as a major global Nd flux to seawater, supporting the findings by Rousseau et al. (2015).
Within the study by Rousseau et al. (2015), a simplified global extrapolation of the Amazon observation of river particle Nd
release suggest that the particulate river source could even be 6-17 times larger than the dissolved, supported further by recent
measurements by Rahlf et al. (2021), who reported large Nd release from river particulates in the estuary of the Congo River.
Although out of the scope of this study, future work with the Nd isotope scheme in FAMOUS could explore the upper bounds
485   of this hypothesis, which would benefit substantially from increased measurements to resolve in greater detail complex
estuarine processes and account for ε_{Nd} variability between dissolved and river particulates (Goldstein and Jacobsen, 1987;
Rousseau et al., 2015). That said, overall, we interpret this result with some caution, as the enhanced river flux may compensate
for the model not resolving complex and highly variable surface processes where most of the observational data are biased
towards (with 38% of observational data concentrated in upper 100 m compared with 11% below 3,000 m). In addition, the
490   scaled river flux may be compensating for biases within the parameterisation of the reversible scavenging, owing to the
simplified nature of the fixed globally uniform particle settling rate, which, as explored by Pöppelmeier et al. (2022) in a
similar scheme parameterisation, may be too high in the upper layers (i.e., there may be lower settling velocities in the surface
mixed layer) due to enhanced turbulence (Chamecki et al., 2019; Noh et al., 2006) and complexation with organic ligands
(Byrne and Kim, 1990), requiring future exploration.

495

Optimising our scheme for skill in simulating both $[Nd]_d$ and ε_{Nd} demonstrably produces better results than prioritising only
$[Nd]_d$ or ε_{Nd} performance, and reveals the complex behaviour in balancing model skill at simulating $[Nd]_d$ and ε_{Nd} as found
previously (Rempfer et al., 2011; Gu et al., 2019; Pöppelmeier et al., 2020a). The Nd inventory in *REF* is closest to the target
$Nd(I)$ of 4.2×10^{12} g, whilst *REF_IC* underestimates (3.16×10^{12} g) and *REF_CONC2* overestimates (4.54×10^{12} g) the
500   inventory. The residence time is similar for *REF* (727 years) and *REF_IC* (711 years), which is predominantly determined by
scavenging efficiency (i.e., $[Nd]_p/[Nd]_d$; Fig. 3), whereas for *REF_CONC2*, τ_{Nd} is 1,341 years, the latter being unphysical given
the observed variations in ε_{Nd} between basins that require a lifetime less that the ocean overturning time (van de Flierdt et al.,
2016). As such, our choice to weight model skill equally in both $[Nd]_d$ and ε_{Nd} favours an optimised scheme that improves
constraints on the external sources to seawater and encompasses a more complete representation of the marine Nd cycle; ε_{Nd}
505   remains key, but $[Nd]_d$ is important for governing vertical isotopic gradients (Siddall et al., 2008; Pöppelmeier et al., 2022).

Our remaining analysis focuses on *REF*, and compares regional distributions of simulated and measured $[Nd]_d$ and ε_{Nd} values in *REF* across different ocean basins to explore model skill in representing key regional features and variance of the modern marine Nd cycle with respect to depth (Fig. 5). Overall, *REF* is successful in simulating the global distributions of $[Nd]_d$,
510 closely matching measurements of increasing concentrations with depth and with a nutrient like increase along the circulation pathway (van de Flierdt et al., 2016; Goldstein and Hemming, 2003), where the highest $[Nd]_d$ (approximately 50 pmol kg^{-1}) occurs in the deep Pacific (below 5,000 m) (Fig. 5b). However, model-data $[Nd]_d$ mismatches occur in the upper 1,000 m across all basins. Here, mean simulated $[Nd]_d$ is underestimated, with the largest underestimations occurring within the uppermost (top 100 m) surface layers, indicating *REF* does not capture fully the measured surface $[Nd]_d$ variability, a feature
515 common amongst previous Nd isotope implementations (Arsouze et al., 2009; Rempfer et al., 2011; Gu et al., 2019, Robinson et al., submitted). We attribute the surface $[Nd]_d$ underestimation to a combination of the low spatial resolution of the model, which limits full representation of point surface inputs (Goldstein and Hemming, 2003), too strong particle scavenging in the surface layers, and/or the misrepresentation of elevated surface and marginal Nd sources.
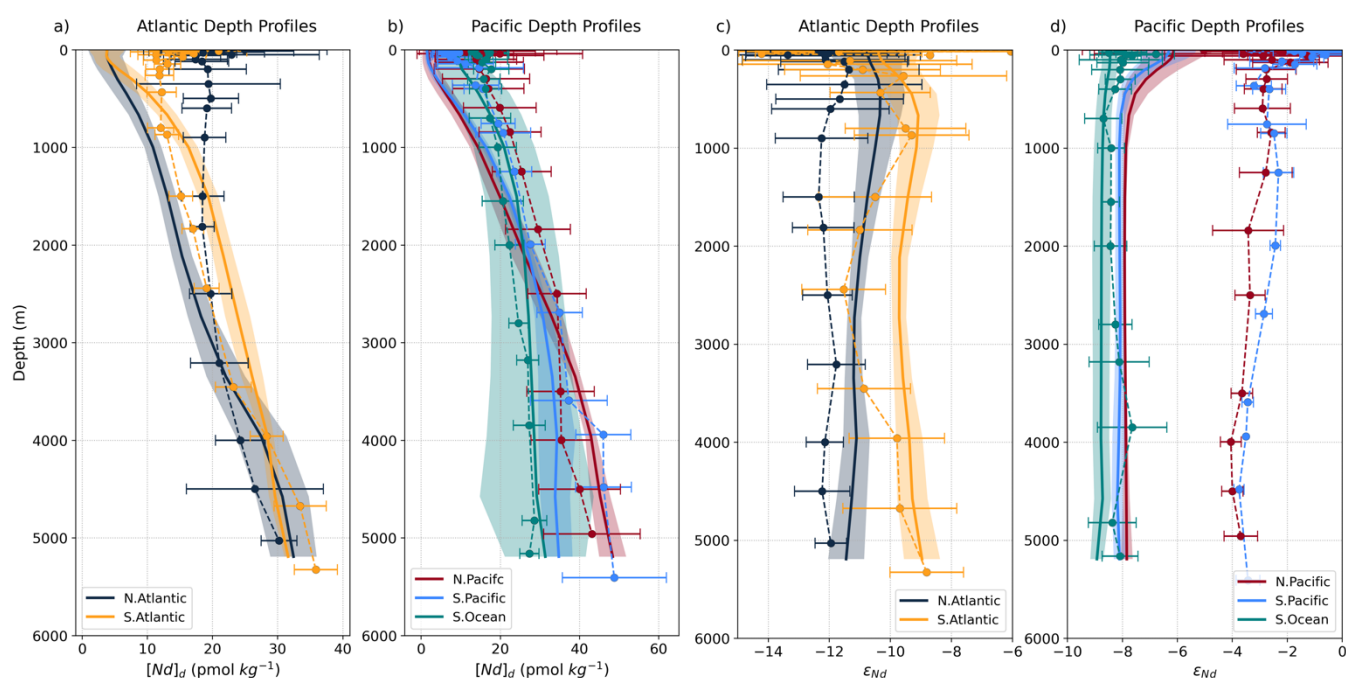
520 **Figure 5: Basin averaged $[Nd]_d$ ((a); North and South Atlantic, (b); North and South Pacific and Southern Ocean) and ε_{Nd} profiles ((c); North and South Atlantic, (d); North and South Pacific and Southern Ocean) with depth in *REF*. The mean and standard deviation of modern seawater measurements (Osborne et al., 2017, 2015; GEOTRACES Intermediate Data Product Group, 2021) are calculated for each vertical grid level and represented by the thinner dashed lines and error bars. The mean and standard deviation of the model are represented by the thicker solid line and lighter coloured ribbon.**

525 Moreover, *REF* slightly overestimates the mean vertical $[Nd]_d$ gradients compared with measurements, particularly in the North Atlantic, where measured $[Nd]_d$ is higher than simulated in the surface to intermediate layers and slightly lower than

simulated at depth (Fig. 5a). Additionally, the measured profiles of $[Nd]_d$ in the upper 3,000 m are more homogenous throughout the water column than simulated. This overestimated vertical gradient implies that in the North Atlantic, high surface Nd inputs fluxes are underestimated, and in regions of deep-water convection, efficient scavenging processes are
530 governing distributions in *REF*, which would otherwise act to homogenise $[Nd]_d$ with depth. In the South Atlantic, below about 500 m, simulated $[Nd]_d$ is a better match to observations, but remains overestimated by approximately 5 pmol kg^{-1} between 1,000 and 3,000 m, and closely matches measurements > 4,000 m below the surface. in conjunction with the North Atlantic comparison, this also hints at there being too much release from reversible scavenging within the ocean's interior in the model. Thus, the rates of desorption of Nd at depth may be too strong, supporting suggestions by Haley et al. (2017) that undue
535 emphasis is imposed on water column desorption as a primary driver of $[Nd]_d$. The inherent complexities and uncertainties regarding reversible scavenging require more detailed evaluations including a better spatial quantification of the modes and rates of scavenging, and dependence on particle type, before any full conclusions can be made (Stichel et al., 2020). The mean $[Nd]_d$ profiles are matched with better skill in the Southern Ocean, although *REF* simulates a higher variability throughout the water column compared to measurements (Fig. 5b). The non-conservative benthic flux sources from Antarctica's margins and
540 seafloor coupled with an internal source via reversible scavenging notably from dissolution of biogenic opal are likely the primary drivers of this variance. *REF* captures the major basinal $[Nd]_d$ distributions in the Pacific, indicating good model skill in representing concentrations in this basin, albeit with a slight overestimation of the vertical gradient in the North Pacific.

Regarding model skill in representing regional ε_{Nd} distributions, simulated ε_{Nd} captures the mean and bulk variance in the depth
545 profiles of the Atlantic and the Southern Ocean, implying the boundary conditions and internal processes driving ε_{Nd} are being suitably represented here (Fig. 5c-d). Surface ε_{Nd} variability is not fully captured in the scheme, and a bias occurs in the North Atlantic, particularly in the Labrador Sea, whereby *REF* does not capture the distinct unradiogenic surface signal (measured ε_{Nd} is -18 compared to simulated values of -11). This potentially arises from the model underestimating the magnitude of surface Nd input, alongside the simplified prescription of ε_{Nd} from the dust and river boundary conditions, or may allude to
550 missing processes, such as the preferential and elevated mobilisation of reactive unradiogenic sediment components driving localised marginal Nd sources. Noticeably, whilst *REF* captures the general depth profile and variance of ε_{Nd} in the Pacific, there is a distinct whole-profile offset, whereby simulated ε_{Nd} is much too unradiogenic (offset by 3 to 4 ε_{Nd}-units) compared to water column measurements, a feature common amongst sophisticated global Nd isotope enabled models (Jones et al., 2008; Arsouze et al., 2009; Rempfer et al., 2011; Gu et al., 2019; Pöppelmeier et al., 2020a). Specifically, we think that biases within
555 the sediment boundary conditions and spatially-uniform fluxes are strong contenders for explaining a large part of the differences between measured and simulated Nd distributions, as they do not capture the regional reactive and radiogenic volcanic features present in the Pacific (Jones et al., 2008; Tachikawa et al., 2017). Future effort is therefore required to constrain such large basinal model-data mismatches if global Nd isotope models are to be used to help resolve instances of ε_{Nd} shifts in the palaeoceanographic records (e.g., Hu and Piotrowski, 2018).

560

Distinct water mass ε_{Nd} properties are represented in *REF*, capturing important features of water mass structure in the Atlantic Ocean (as illustrated in the Atlantic stream function plot in Fig. 6a). For example, the vertical Atlantic ε_{Nd} cross-section at around 35° S co-varies with salinity and shows southward flowing NADW with ε_{Nd} of -11.2, underlain by northward flowing Antarctic Bottom Water (AABW) with ε_{Nd} of -10.8 (Fig. 6b), encompassing the canonical Atlantic zig-zag profiles of ε_{Nd}

565   (Goldstein and Hemming, 2003). These distinct water mass tracer properties make *REF* a suitable simulation to explore the varying influences of northern and southern sourced water masses in the Atlantic, which is required to aid in palaeoceanographic reconstructions and their interpretation. However, simulated NADW is more radiogenic than indicated by water column measurements (where lower NADW ε_{Nd} is -12.4; Lambelet et al., 2016), suggesting that Nd source distributions for this water mass require further constraints. Moreover, ε_{Nd} is shifted to greater depths compared to corresponding salinity

570   (Fig. 6b). This dissimilarity results from reversible scavenging processes, whereby adsorption and subsequent desorption of Nd with particle dissolution causes a non-conservative downward transport of ε_{Nd} (Rempfer et al., 2011; Pöppelmeier et al., 2022; Siddall et al., 2008). Moreover, the benthic flux contributes a less radiogenic source to AABW along its northward bottom water flow path and causes a shift in ε_{Nd} signal towards values which are more similar to that of NADW. This vertical ε_{Nd} offset, which has also been directly observed in the modern South Atlantic (Wang et al., 2021), indicates that the rates of

575   particle dissolution and scavenging efficiency are major vertical processes acting throughout the water column. Here, the concentration mixing dynamics (whereby vertical processes occurring in abyssal water masses with a high $[Nd]_d$ will have a weaker effect on ε_{Nd} than intermediate masses with a comparably low $[Nd]_d$) can help explain the 'Nd paradox' (Siddall et al., 2008; Pöppelmeier et al., 2022).
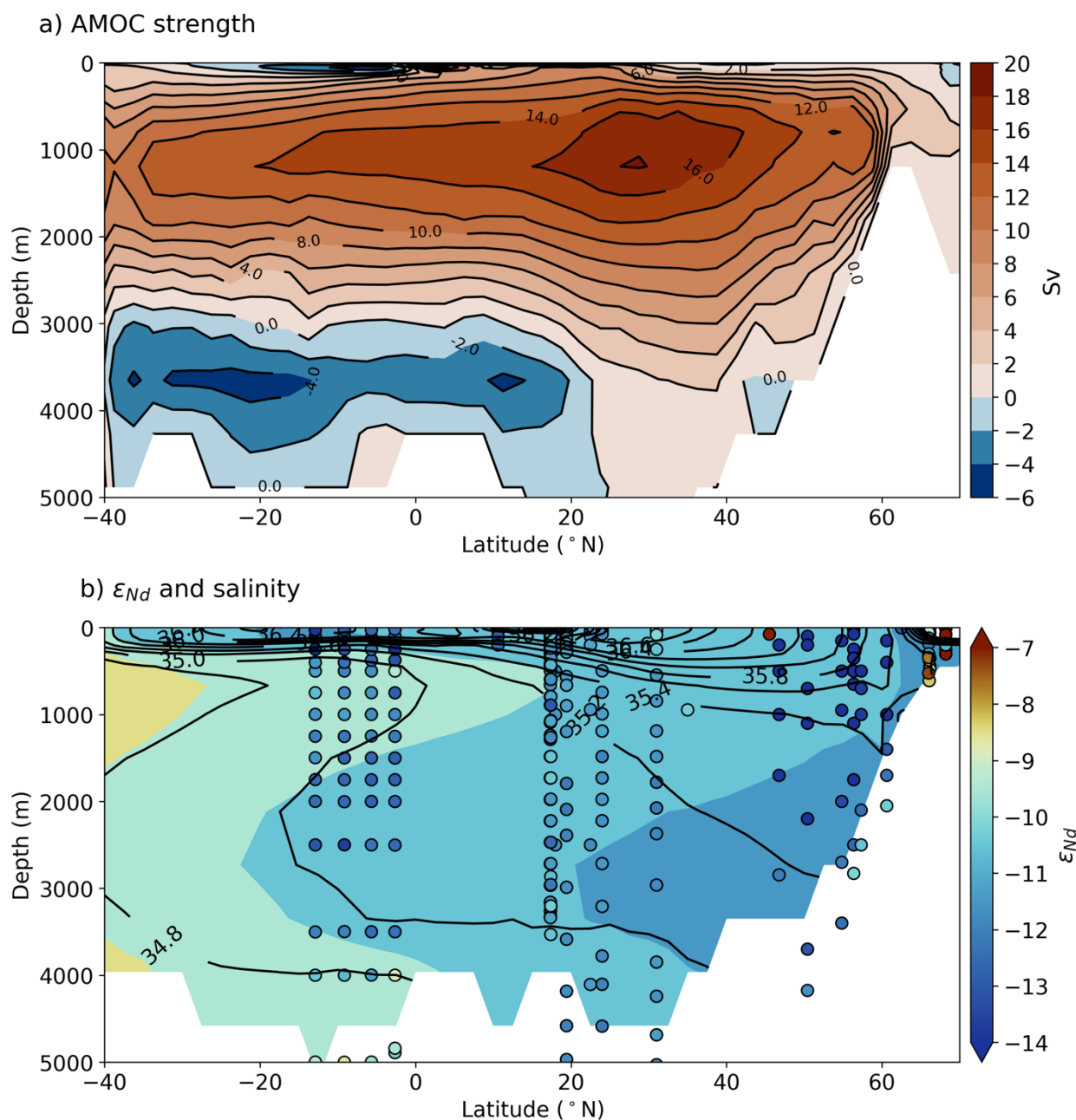
Figure 6: The conservative water mass tracer properties of ε_{Nd} in the optimised *REF* simulation in the Atlantic Ocean, as indicated by (a) zonally integrated Atlantic Ocean stream function (Sverdrup, Sv; where 1 Sv = 10^6 m^3 s^{-1}), (b) simulated ε_{Nd} (coloured) and salinity (contours) in a cross section of the Atlantic (averaged across 20-30 ºW), compared to water column measurements of ε_{Nd} (filled circles using the same colour scale).

Overall, we conclude that *REF* has skill in representing the global distributions and key features of both $[Nd]_d$ and ε_{Nd}, including

the ε_{Nd} of distinct water masses in the Atlantic. Deviations in $[Nd]_d$ and ε_{Nd} from the observational data vary regionally, and

can be typically attributed to the resolution of FAMOUS, alongside highlighting certain inconsistencies within the assumptions underlying the Nd inputs to seawater, which, due to the inherent elusive nature of marine Nd cycling, still remain preliminary approximations of complex sediment-seawater interactions. We suggest that future modelling and observational studies should focus on resolving upper ocean sources of Nd where the largest model-data disparity occurs, and further on improving the

590   representation and spatial extent of labile seafloor ε_{Nd} interactions, including exploring in detail the regional differences in how seawater acquires a ε_{Nd} signal (i.e., the interplay of Nd additional versus advection time). The optimised parameters in *REF* allow for ease of future model improvements, which may include updating model ε_{Nd} source boundary conditions subject to increased measurements and more quantitative process descriptions, alongside testing outstanding questions regarding marine Nd cycling and ocean circulation. Altogether, we argue that *REF* is a well-designed tool capable of improving the application

595   of Nd isotopes as an ocean circulation tracer.

4. Sensitivity of optimised *REF* simulation to seafloor sediment ε_{Nd} distributions

To investigate the influence of varying regional reactive ε_{Nd} sources on simulated seawater Nd isotope distributions, caused by the potential preferential mobilisation of certain components of the sediment, we performed idealised sensitivity tests using our optimised *REF* simulation. We tested three different sediment maps (i.e., sediment boundary conditions shown in Fig. 7:a-

600   c) in simulations *REF*, *REF-SED2* and *REF-SED3*, representing the ε_{Nd} distributions of reactive sediment under a seafloor-wide benthic flux model of marine Nd cycling. The rationale for exploring a shift in sedimentary ε_{Nd} towards more extreme values is based upon evidence from a combination of laboratory analysis, seawater and porewater measurements, and modelling studies that demonstrate a substantial relabelling of water masses by a benthic source. These pieces of work suggest that the bulk ε_{Nd} of the sediment cannot always be assumed to represent the mobile sedimentary ε_{Nd} phase governing

605   distributions of seawater ε_{Nd} (Abbott et al., 2015a; Wilson et al., 2013; Du et al., 2016; Lacan and Jeandel, 2005b; Jones et al., 2008; Pearce et al., 2013; Rousseau et al., 2015; Abbott et al., 2016; Jeandel and Oelkers, 2015). Note, however, that our sensitivity analyses are designed to be quasi-idealised (i.e., simplified) end-member tests of some of the major assumptions implicit to paradigms pertaining to the mobility/exchangeability of seafloor Nd, as explained below, and are not meant to provide a redefined seafloor ε_{Nd} boundary condition for models. Like the optimisation simulations (Sect. 2.2), dissolved

610   seawater Nd in all sensitivity studies is initialised from zero, and integrated for 6,000 years to enable the deep ocean and seawater Nd to reach steady state.

The first map of global ε_{Nd} distributions at the sediment-ocean interface (*REF*: Fig.7a) represents the estimated bulk ε_{Nd} distributions of the continental margins and seafloor detrital material of Robinson et al., 2021 (see their Figure 4). The

615   subsequent two maps (*REF-SED2*: Fig. 7b and *REF-SED3*: Fig. 7c) impose simplified modifications of increasing magnitude to the soluble ε_{Nd} from localised sediment regions in the Pacific (particularly across the eastern and western margins, where we cap the regional ε_{Nd} signal by imposing a minimum threshold; causing the sediment region to become more *radiogenic*),

and in the Atlantic Ocean (particularly the Northwest Atlantic, where we cap the regional ε_{Nd} signal by imposing a maximum threshold; causing the sediment region to become less *radiogenic*); see Supplementary Table S3 and Text S1 for the specific

620   definition and choice of the regional sediment ε_{Nd} thresholds. All other model parameterisations are from the optimised *REF* simulation and are the same amongst the sensitivity simulations. Thus, because the magnitude of Nd sources are fixed, $[Nd]_d$ does not vary between simulations and so here we focus our discussion on changes to seawater ε_{Nd} distributions.
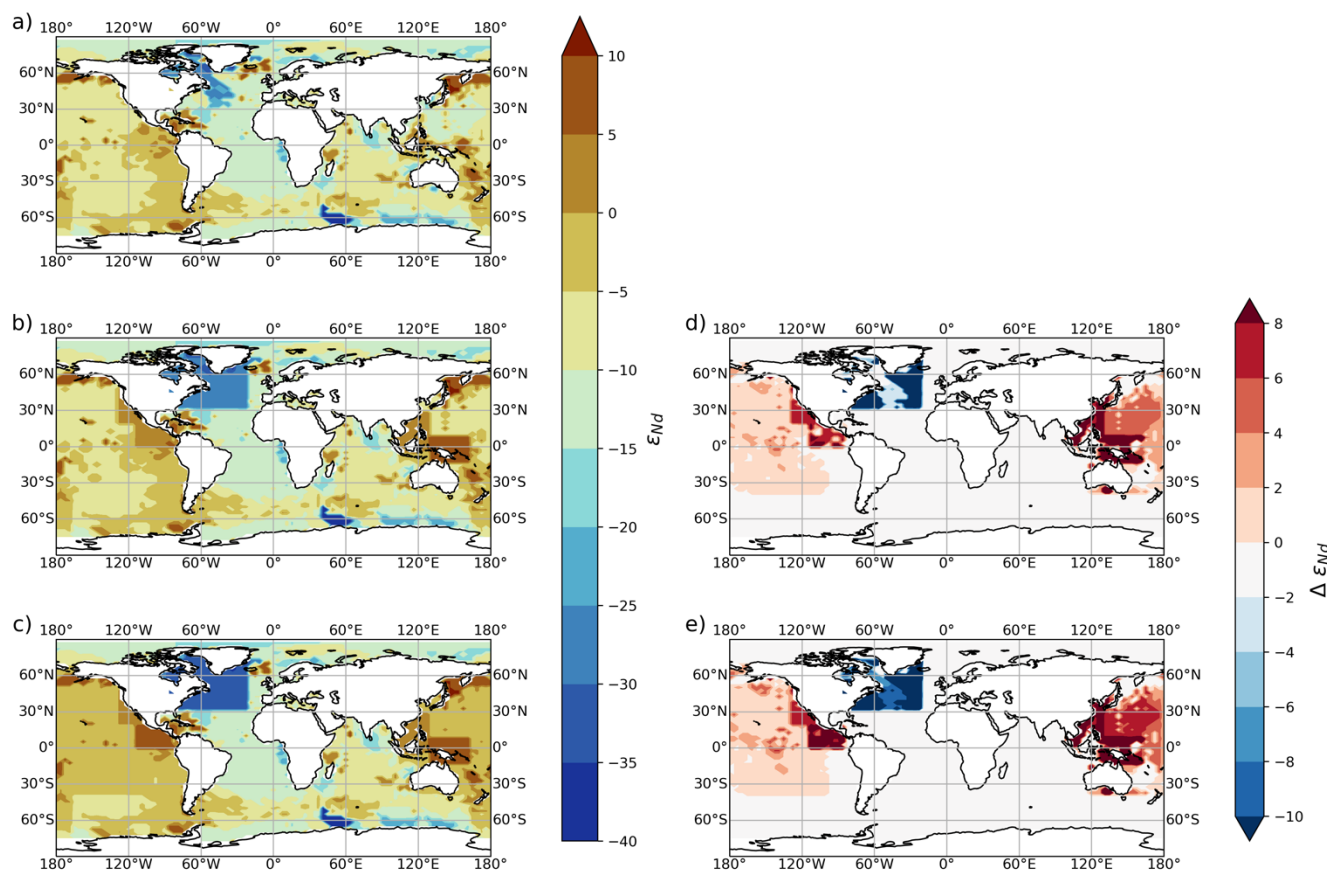
Figure 7: Global sediment ε_{Nd} distributions at the sediment-water interface used to represent the seafloor benthic flux under
625   **sensitivity studies testing (a; *REF*) the bulk sediment ε_{Nd} signal as presented in Figure 4; Robinson et al. (2021), and (b; *REF-SED2***
and c; *REF-SED3*) representing two modified sediment ε_{Nd} maps of increasing magnitude to test the hypothesis that certain reactive
sedimentary phases dominate sediment-seawater interactions. The difference between the modified ε_{Nd} maps and the bulk sediment
map (a) are shown on the adjacent right-hand side plots (d-e), in ε_{Nd}-unit difference. See Supplementary Fig. S3 for ε_{Nd} distributions
on the FAMOUS GCM grid which are directly input as sediment boundary conditions in the Nd isotope scheme.

630   Modifying the ε_{Nd} distributions of the labile seafloor sediment influences the model's skill at representing modern measurements as indicated by the returned MAE ε_{Nd} cost functions ($J_{\varepsilon Nd}$: Table 4), demonstrating that the heterogeneity of sediment reactivity and isotopic composition likely plays an important role in the oceanic cycling of Nd isotopes (Du et al., 2016; Wilson et al., 2013; Abbott et al., 2016). Here, the global $J_{\varepsilon Nd}$ is reduced from 2.37 ε_{Nd}-units in *REF* to 2.22 ε_{Nd}-units in

REF-SED3. In other words, adjusting the seafloor ε_{Nd} to take account of the enhanced reactivity of particular sediment phases,
which may have more extreme ε_{Nd} signatures than the bulk sediment, improves model skill; 73% of measurements in *REF-SED3* are simulated within 3 ε_{Nd}-units, compared to 67% in *REF*. As expected, varying the seafloor sediment distributions did not impact global model skill noticeably above 1,000 m, but improved skill at intermediate and deep depths below (Table 4). In more detail, the Pacific Ocean basin has a large $J_{\varepsilon Nd}$ of 3.98 ε_{Nd}-units under bulk sediment boundary conditions (i.e., *REF*), which is improved under *REF-SED3* to 3.04 ε_{Nd}-units. In contrast, despite substantially more unradiogenic reactive sediment distributions applied in the North Atlantic compared to the bulk (with maximum ε_{Nd} values capped at -28 and -34 within the mobile sediment in *REF-SED2* and *REF-SED3* respectively, equating to localised differences of over -10 ε_{Nd}-units: Fig. 7d-e), model skill in representing Atlantic ε_{Nd} is relatively insensitive to these changed boundary conditions. Overall, we observe a slight decrease in Atlantic model skill, where $J_{\varepsilon Nd}$ is 1.63 ε_{Nd}-units in *REF* and 1.84 ε_{Nd}-units in *REF-SED2* (Table 4). Furthermore, the $J_{\varepsilon Nd}$ of the Southern Ocean is sensitive to changing sediment ε_{Nd} distributions in the North Atlantic and Pacific basins, and model skill decreased here under the more extreme sediment ε_{Nd} boundary conditions (where $J_{\varepsilon Nd}$ is 0.52 and 1.12 ε_{Nd}-units in *REF* and *REF-SED3* respectively), whilst the Arctic and Indian Oceans are relatively insensitive. We delve into the reasons for such responses and explore spatial seawater ε_{Nd} distributions in more detail below.

Table 4: Overview of general model skill of the three sensitivity studies exploring labile seafloor sediment ε_{Nd} distributions. Displaying global and regional mean absolute error for ε_{Nd} (MAE:$J_{\varepsilon Nd}$)

Simulation	$J_{\varepsilon Nd}$ global (n=2,475)	% within 3 ε_{Nd}-units	$J_{\varepsilon Nd}$ surface (0-200 m)	$J_{\varepsilon Nd}$ shallow (200-1,000 m)	$J_{\varepsilon Nd}$ mid-depth (1,000-3,000 m)	$J_{\varepsilon Nd}$ deep (>3,000 m)	$J_{\varepsilon Nd}$ Atlantic	$J_{\varepsilon Nd}$ Pacific	$J_{\varepsilon Nd}$ Indian	$J_{\varepsilon Nd}$ Southern Ocean	$J_{\varepsilon Nd}$ Arctic
REF	2.37	67	2.68	2.26	2.32	1.68	1.63	3.98	2.88	0.52	1.82
REF-SED2	2.26	71	2.59	2.18	2.18	1.52	1.86	3.18	2.94	0.98	1.81
REF-SED3	2.22	73	2.58	2.16	2.09	1.43	1.84	3.04	2.94	1.12	1.80

What we learn from the performance of *REF-SED2* and *REF-SED3* relative to *REF*, is that increasing the mobilisation of radiogenic sediment in the Pacific relative to the bulk drives Pacific seawater ε_{Nd} distributions towards more radiogenic values in slightly better agreement with measurements (Fig. 8). In the abyssal North Pacific, between *REF*, where seawater ε_{Nd} is -7.5, and *REF-SED3*, where seawater ε_{Nd} is -5.5, there is a change of +2 ε_{Nd}-units (Supplementary Fig. S4). This is the largest shift in the magnitude of major water mass end member ε_{Nd} within all of the sensitivity simulations. The rest of the interior of the Pacific undergoes more modest changes of +1 to +2 ε_{Nd}-units, resulting from lateral and diapycnal mixing of the benthic flux signal throughout the water column. The results here broadly support the notion that preferential mobilisation of certain more reactive and more radiogenic phases (e.g., volcanic ash) within detrital sediment occurs during early diagenesis (Du et al., 2016; Abbott et al., 2015b, a, 2016; Wilson et al., 2013). This labile Nd source, which is more radiogenic than the bulk ε_{Nd}, interacts with deep waters via a benthic flux and is necessary to explain in part the observed radiogenic change in Pacific deep water ε_{Nd} along its sluggish northward flow path in the absence of deep-water formation (Haley et al., 2017).

However, even under the considerably radiogenic Pacific sediment forcing applied in *REF-SED3* (where minimum labile

665 seafloor sediment ε_{Nd} values are regionally capped at +8 and +10 across the western and eastern equatorial Pacific respectively; Fig. 7c), the general Pacific ε_{Nd} signal of -6 (Fig. 8c) is still too unradiogenic compared to average water column measurements of -4 ε_{Nd} in the North Pacific (Amakawa et al., 2009; Fuhr et al., 2021; Behrens et al., 2018; Fröllje et al., 2016), and especially in the upper 2,000 m (where seawater ε_{Nd} measurements are -2.5). This implies a missing or misrepresented highly radiogenic Nd source, possibly capturing strong local particle-seawater exchange occurring in the upper and intermediate ocean. This

670 finding is supported by suggestions of highly localised non-conservative Pacific ε_{Nd} behaviour at depths between 0 and 1,500 m and within 1,000 km of coasts, including radiogenic offsets from conservative mixing in intermediate waters close to Hawaii, along the eastern coast of Japan, and margins along the eastern equatorial Pacific (Tachikawa et al., 2017). Our results imply that these marginal volcanic sediment sources, close to continental inputs with high detrital and biogenic particle concentrations (that drive strong particle-seawater interactions), may govern marine ε_{Nd} distributions in the North Pacific. As

675 such, these shallower and marginal regions may pose a larger in magnitude and more distinct Nd source to seawater as opposed to an open-ocean abyssal benthic source; increased measurements at these locations would therefore greatly improve our understanding of this re-labelling.
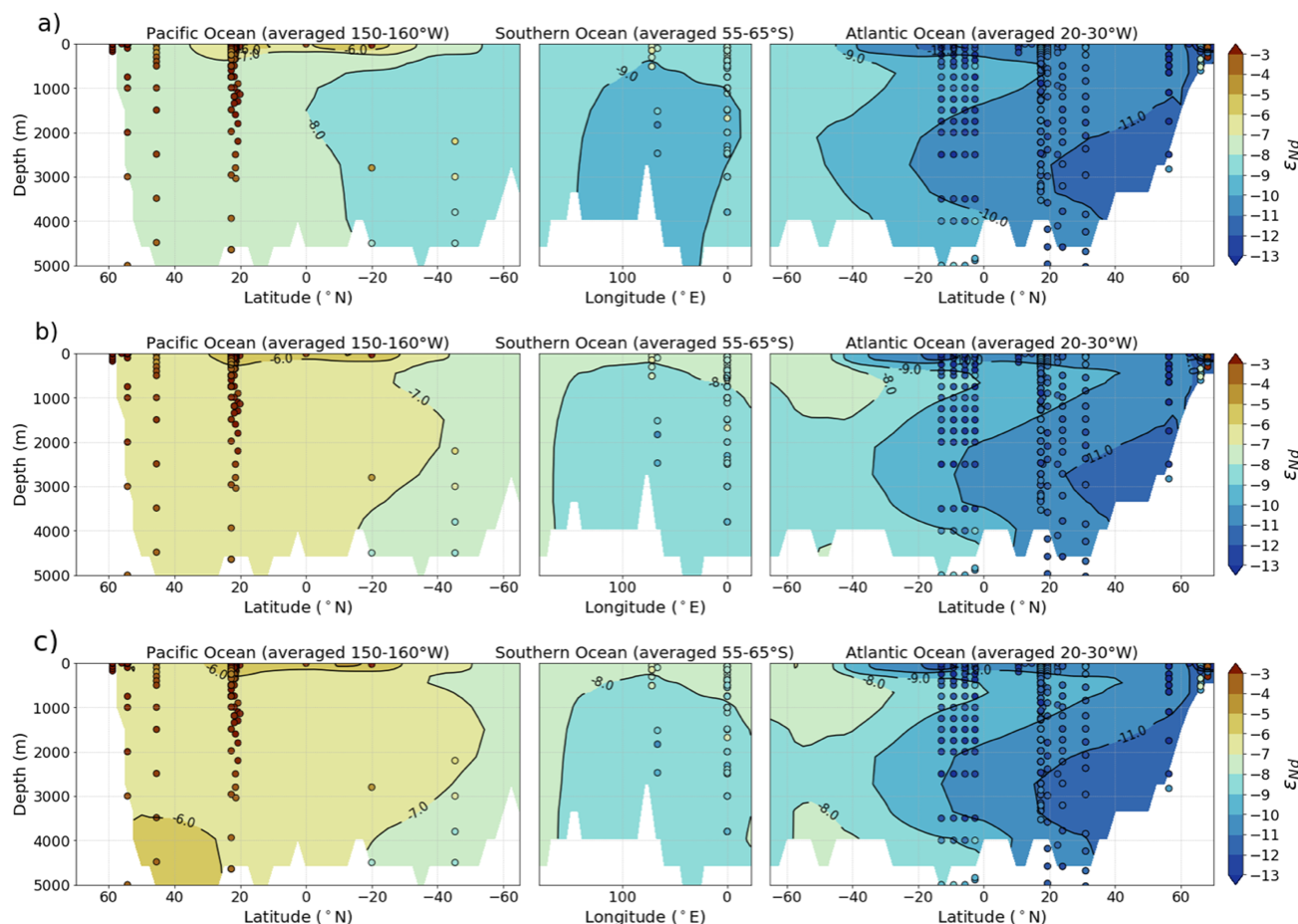
Figure 8: Vertical sections of simulated ε_Nd within three seafloor sediment ε_Nd sensitivity studies (a) *REF*, (b) *REF-SED2*, and
(c) *REF-SED3* along a transect from the Pacific to Atlantic, traversing the Southern Ocean from West to East. Water column
measurements are imposed as filled circles using the same colour scale. Simulated and measured ε_Nd from the Pacific are from 150-
160° W, in the Southern Ocean are from 55-65° S, and in the Atlantic values are from 20-30° W.

On the other hand, the more unradiogenic reactive North Atlantic sediment ε_Nd distributions imposed in *REF-SED2* and *REF-*

SED3 (relative to the bulk sediment reconstruction used in *REF*) produces only slightly less radiogenic ε_Nd that are highly

685   localised to the abyssal northern North Atlantic, with a change of -0.4 ε_Nd-units between *REF* and *REF-SED3* (Fig. 8 and

Supplementary Fig. S4). The remaining Atlantic areas bathed in NADW experience a small adjustment towards more

radiogenic values, a response to the radiogenic Nd sourced in the Pacific propagating into the Atlantic. Here simulated ε_Nd

range between -11 to -10, resulting from a shift of +0.2 to +0.8 ε_Nd-units in NADW in *REF-SED2* and *REF-SED3* respectively

when compared with *REF*. It may be that the less radiogenic sediment ε_Nd forcing in the North Atlantic is required to counter

690   the more radiogenic southern-sourced water, and without such a source, the entire Atlantic could shift to more radiogenic

values; future simulations exploring the response of seawater ε_Nd to only the Pacific (or the Atlantic) sediment adjustments

would be best suited to explore this. However, this localised and minor shift of ε_Nd under less radiogenic seafloor benthic fluxes

in the North Atlantic (in *REF-SED2* and *REF-SED3*) implies a weak sensitivity of NADW ε_{Nd} to forcing from a localised abyssal benthic flux, where the somewhat positive response is governed by northward mixing from more radiogenic waters from the Southern Ocean. We thus find evidence that these bottom-water sediment regions are not important for governing Atlantic ε_{Nd}, likely because vigorous advection across the seafloor inhibits the exposure time of seawater to relabelling by a benthic flux. Therefore, most of the modern Atlantic ε_{Nd} signal is pre-formed. Further model experiments with sluggish Atlantic circulation could verify this, but we postulate that Atlantic seawater ε_{Nd} experiences an overriding influence from distinct and reactive unradiogenic surface and marginal Nd inputs, around key regions of deep-water formation, such as in the Labrador Sea. This likelihood is brought to the fore by *REF-SED3*, where NADW remains too radiogenic despite a large unradiogenic forcing applied across the seafloor, indicating here the benthic flux signal does not act to relabel seawater ε_{Nd} markedly along its flow path, and so does not exert a strong control on water column ε_{Nd} distributions (Fig. 8c). Thus, it follows that accurate quantification of the mobile abyssal seafloor sedimentary phases may be of secondary importance in the modern North Atlantic. Instead, we suggest that future studies should be focussed on resolving upper-intermediate Atlantic Ocean Nd source isotope distributions (e.g., the magnitude and interactions from river sourced particulate material, alongside quantifying the fluxes from areas of intense boundary exchange occurring via sediment-seawater interactions with freshly eroded material near the margins). Nonetheless, the impact of a benthic flux on North Atlantic seawater ε_{Nd} distributions may be different under changed circulation regimes in the Atlantic, which thus require future explorations.

Finally, in the Southern Ocean, where the Antarctic Circumpolar Current (ACC) vigorously merges the waters from the Atlantic, Pacific and Indian Oceans, seawater ε_{Nd} experiences a shift to more radiogenic values under the modified sediment simulations (Fig. 8). Here, the general Southern Ocean ε_{Nd} signal increases from -9 in *REF* to -8.2 in *REF-SED2*, and to -8 in *REF-SED3*. The larger spatial extent of the labile sediment modifications in the Pacific compared to the Atlantic (Fig. 7), coupled with the higher-amplitude absolute response of Pacific seawater ε_{Nd} in the sensitivity simulations drives this radiogenic shift in the ε_{Nd} in the Southern Ocean. Consequently, the endmember ε_{Nd} of Antarctic Intermediate Water (AAIW) and AABW protruding into the South Atlantic (Fig. 8) is most radiogenic in *REF-SED3*, amplifying the distinctions between AAIW, NADW and AABW, and enhancing the South Atlantic zig-zag profiles (Goldstein and Hemming, 2003).

Overall, we consider *REF-SED3* – a simulation with optimised parameters (i.e., *REF*; Sect. 3.2) and an updated sedimentary boundary condition (Fig. 7c), which form a preliminary first-order coarse-scale representation of large scale labile sedimentary phases – to have the highest model skill within the sensitivity studies in capturing $[Nd]_d$ and ε_{Nd} distributions (Fig. 9). This simulation is capable of representing with good fidelity the spatial distributions of modern seawater Nd measurements and supports the preferential mobilisation of reactive radiogenic volcanic sedimentary components in the Pacific relative to the bulk ε_{Nd} under a seafloor-wide benthic-flux driven model of marine Nd cycling. Yet simulated Pacific ε_{Nd} in *REF-SED3* overall remain too unradiogenic. Future work could therefore explore the possibility of more spatially heterogeneous and isotopically

unique benthic fluxes. For example, whereby volcanic material, which is more soluble than well crystalised detrital fractions, may favour elevated benthic fluxes with substantial radiogenic Nd release.
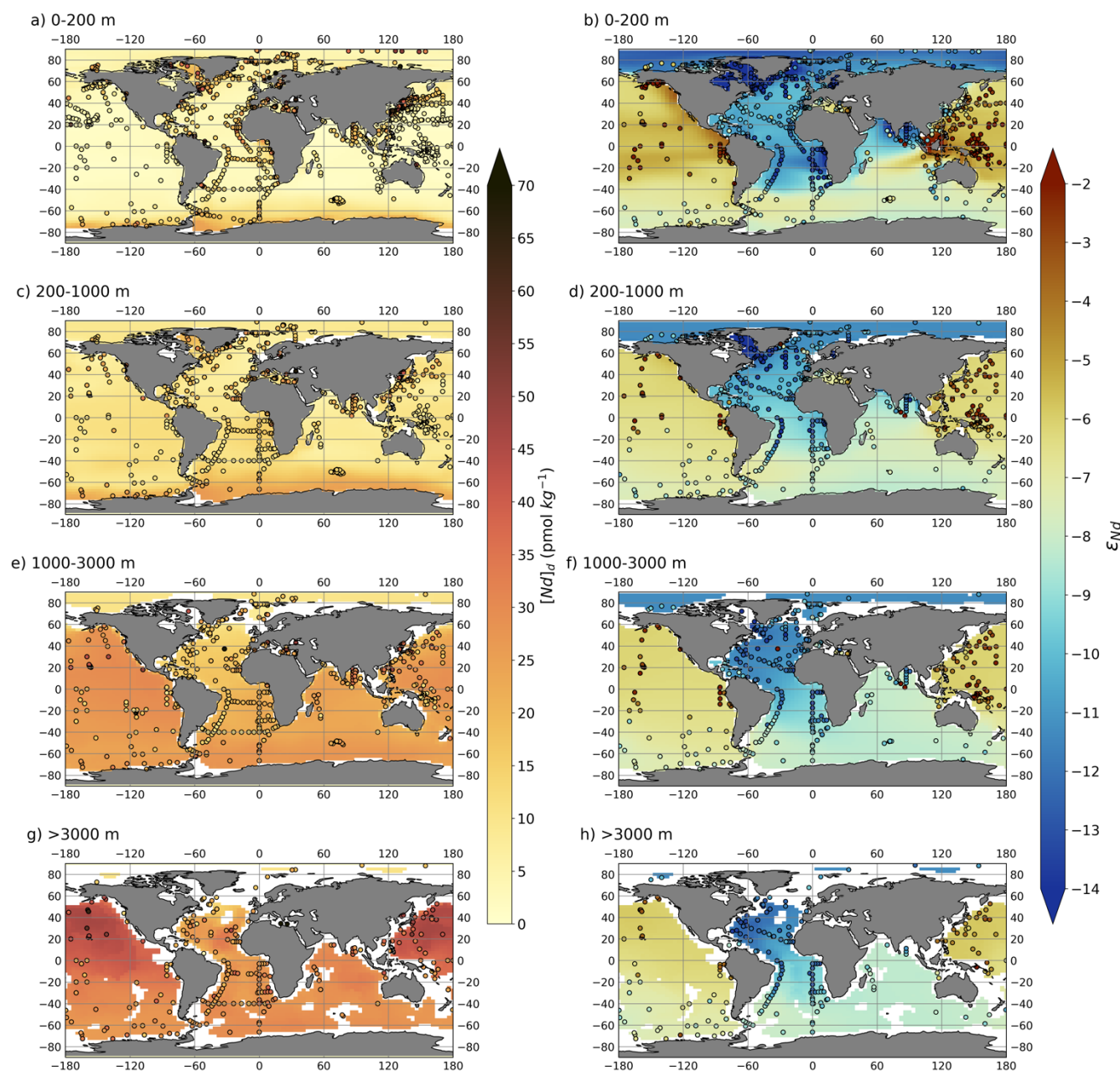
Figure 9: Global volume-weighted distributions of [*Nd*]*d* (left) and ε*Nd* (right) in the optimised simulation *REF-SED3* split into four different depth bins, (a-b) shallow (0-200 m), (c-d) intermediate (200-1,000 m), (e-f) deep (1,000-3,000 m), and (g-h) deep abyssal ocean (>3,000 m). Water column measurements from within each depth bin (Osborne et al., 2017, 2015; GEOTRACES Intermediate Data Product Group, 2021) are superimposed as filled circles using the same colour scale.

730

5. Sensitivity of seawater ε$_{Nd}$ to a margin constrained versus a seafloor-wide benthic flux

In order to further explore the sensitivity of seawater ε$_{Nd}$ distributions to non-conservative seafloor fluxes, we investigated the difference in simulated marine Nd isotope distributions between a continental margin constrained versus a seafloor-wide

735 benthic flux whilst all other parameters were kept constant. At present, it remains undetermined, and even disputed, whether the chemical transfer of Nd between terrestrial derived particles and seawater occurs predominantly across continental margins (proximal to large inputs of distinct and compositionally less mature lithogenic sediment, high eddy kinetic energy, and high detrital and biogenic particle concentrations promoting rapid exchange reactions: Lacan and Jeandel, 2005b; Jeandel and Oelkers, 2015; Tachikawa et al., 2003; Jeandel, 2016; Rousseau et al., 2015), or across the abyssal seafloor (with high particle

740 reactivities and long term benthic flux exposures of fine-grained sediment ubiquitously spread throughout the global ocean: Abbott et al., 2015b, 2019; Du et al., 2016; Abbott, 2019). Hence, we performed a final simulation, using the optimised parameters and updated mobile sediment ε$_{Nd}$ boundary conditions from *REF-SED3* (Sect. 4), but with the sediment source constrained specifically to the continental margins (where sediment thickness ≥ 1,000 m, following the continental margin definition by Robinson et al. (2021)), we call this simulation *REF-SED3-MG*. See Supplementary Fig. S7 for the gridded ε$_{Nd}$

745 sedimentary distributions of the margin-only flux. In this simulation, f_{sed} is redistributed to the margins proportional to the surface area, where the constant sediment flux across the margins is 30.75 pmol cm^2 yr^{-1} (compared to a flux of 2.96 pmol cm^2 yr^{-1} when the flux is integrated across the entire ocean floor). As such, $[Nd]_d$ is generally more concentrated above 3,000 m depth and in the Atlantic and Southern Ocean compared to distributions under a seafloor-wide benthic flux (see Supplementary Fig. S8 for the difference in $[Nd]_d$ between the simulations); note here the following discussion is focussed on exploring Nd

750 isotope distributions and does not explore these differences to $[Nd]_d$ in further detail.

Overall, there is a marked difference in the response of seawater ε$_{Nd}$ distributions between the Atlantic and Pacific basins under simulations with a seafloor-wide (*REF-SED3*) and a margin-only (*REF-SED3-MG*) marine sediment flux (Fig. 10). In the North Pacific, a benthic flux across the entire seafloor results in a more radiogenic seawater ε$_{Nd}$ signal of -6, which sits closer

755 to seawater measurements of -4 (Amakawa et al., 2009; Fuhr et al., 2021; Behrens et al., 2018; Fröllje et al., 2016) compared to when the sediment Nd source is only constrained to the margins (where seawater ε$_{Nd}$ is -8.5). The largest response of seawater ε$_{Nd}$ occurs in the abyssal North Pacific (Fig. 10 and Supplementary Fig. S11), and herby reiterates the importance of a benthic flux in governing seawater ε$_{Nd}$ within the North Pacific, characterised by long-term exposure of bottom waters, with long water residence times, to a radiogenic Nd flux from fine-grained sediment of volcanic origin (Abbott et al., 2015a, b; Du

760 et al., 2016; Abbott et al., 2016; Haley et al., 2017; Behrens et al., 2018). Moreover, under the margin-only simulation (*REF-SED3-MG*), the missing benthic Nd source and lack of radiogenic input into the Pacific results in the Southern Ocean ε$_{Nd}$ signal, which is determined in part by mixing of these Pacific waters, becoming too unradiogenic (where simulated ε$_{Nd}$ is -10: Fig. 10b) compared to measurements (where ε$_{Nd}$ is -8.5: Stichel et al., 2012; Lambelet et al., 2018).
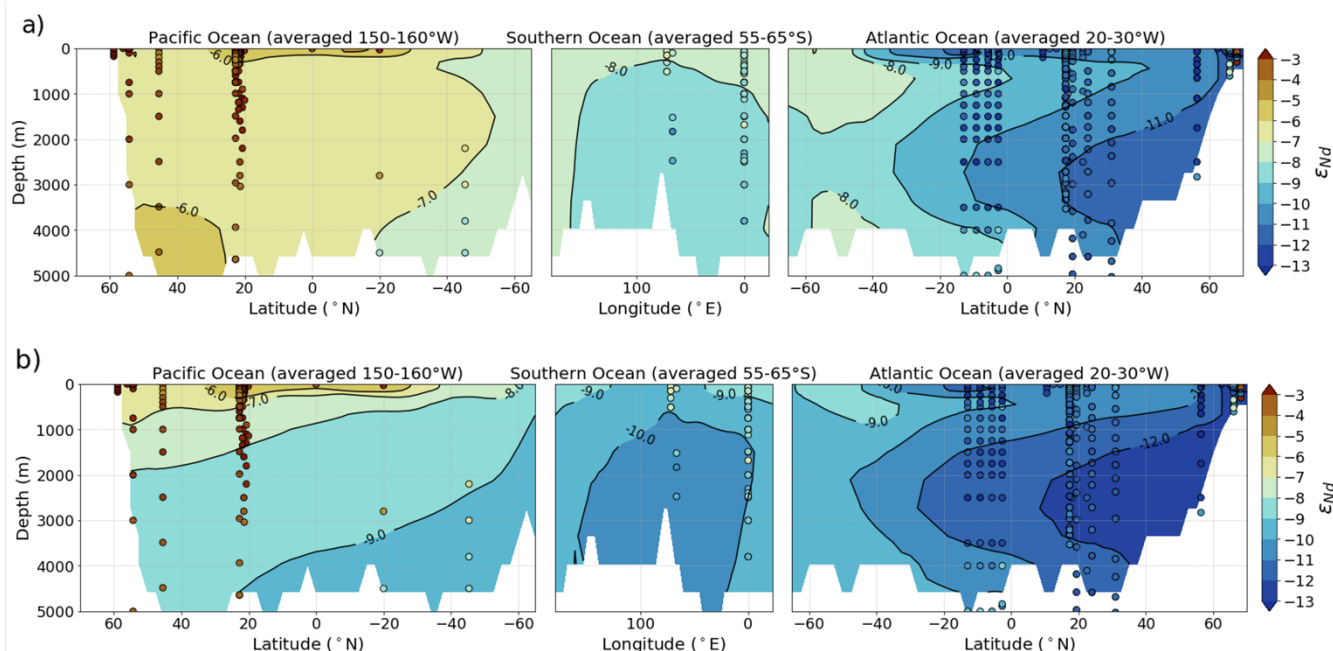
Figure 10: Vertical sections of simulated ε_{Nd} within sensitivity studies (a) *REF-SED3 with a seafloor-wide* **benthic flux and (b)** *REF-SED3-MG* **with a** *margin-only* **constrained benthic flux along a transect from the Pacific to Atlantic, traversing the Southern Ocean from West to East. Water column measurements are imposed as filled circles using the same colour scale. Simulated and measured ε_{Nd} from the Pacific are from 150-160° W, in the Southern Ocean are from 55-65° S, and in the Atlantic values are from 20-30° W. The continental margins are constrained following the definition by Robinson et al. (2021), where sediment thickness ≥ 1,000 m.**

In contrast, the North Atlantic, characterised by high modern ventilation rates, displays a limited expression of non-conservative behaviour from seafloor benthic fluxes (Fig. 10). Here, a margin-only constrained benthic flux improves model-data fit, resulting in a more unradiogenic NADW ε_{Nd} signal of -13, which is in excellent agreement with measurements for this water mass of -13.2 (Lambelet et al., 2016), compared with -11 simulated under a seafloor-wide benthic flux. Resolving the ε_{Nd} signal of modern NADW therefore primarily resides within disentangling the highly reactive and isotopically unique surface and marginal Nd fluxes (i.e., intense localised regions of boundary exchange), especially around the locations of deep-water formation, including unradiogenic inputs originating from the Canadian Shield (where ε_{Nd} is -28), to localised radiogenic inputs from Icelandic basaltic rocks (where ε_{Nd} is +7) (Blaser et al., 2019b; Stichel et al., 2020; Morrison et al., 2019; Lacan and Jeandel, 2005a; Lambelet et al., 2016). Furthermore, mixing of the less radiogenic southern-sourced water in the Atlantic likely also contributes to the more unradiogenic signal of NADW under a margin-only constrained benthic flux.

To summarise, the ε_{Nd} signal of modern bottom waters within the Pacific Ocean are sensitive to abyssal benthic flux alterations, whilst bottom water in the North Atlantic displays a much weaker response. Our results demonstrate the importance of setting apart the interlinked roles of major sediment Nd sources (their ε_{Nd} composition, spatial extent, and reactivity), from physical

785 ocean circulation structure (provenance of water masses and sites of convection, water ventilation rates and residence time). It would therefore be beneficial for future work to focus on further disentangling regional environmental conditions and how they may influence non-conservative marine Nd isotope behaviour (e.g., constraining pore water redox conditions, productivity, oxygenation, and pH, and how those conditions may drive benthic Nd fluxes). Moreover, future work could explore the response of seawater ε_{Nd} distributions to different definitions of the continental margin extent (e.g., where sediment
790 thickness ≥ 500 m; Fig. S5 of Robinson et al. (2021)).

Henceforward, the sensitivity simulations presented here provide a foundation for future work with the Nd isotope scheme in the FAMOUS GCM to further investigate and attempt to identify the environmental qualities and spatial regions of seafloor sediment that likely result in mobilised benthic fluxes within regions that dominate seawater ε_{Nd} distributions over water mass
795 mixing in the deep ocean. This would largely benefit from increased direct measurements of pore water Nd concentration and isotopic composition alongside a greater understanding of the diagenetic Nd cycle and the role of reversible scavenging processes. Combined with such 'observations', the modelling framework presented here would allow for the crucial disentangling of non-conservative processes involved in governing distributions of marine ε_{Nd}. Based on our results, we contend that the existence of such limitations in our knowledge is perhaps overconfidently dismissed in the application of
800 marine Nd isotopes as an ocean circulation and continental weathering tracer.

Finally, we do wish to highlight that our results in Sect. 4 and 5 only look at the influence of mobilised seafloor ε_{Nd} distributions on seawater ε_{Nd} and do not attempt to explore how varying these fluxes may overprint the signal of marine archives. Furthermore, we do not assess the sensitivity of seawater ε_{Nd} distributions to modified benthic fluxes under different circulation
805 regimes (i.e., under a weakened AMOC or an enhanced PMOC). These constitute logical next steps in marine Nd isotope modelling.

6. Summary and Conclusions

In this study, we extended the implementation of Nd isotopes (^{143}Nd and ^{144}Nd) in the ocean component of the FAMOUS GCM by statistically optimising the selected combination of model parameter values to produce a tuned reference simulation
810 for future investigative work with the scheme. Within our experimental design we found that the reversible scavenging, benthic flux magnitude and riverine source scaling all governed the variability in simulated total Nd inventory. The reversible scavenging efficiency dominated the variation in the residence time, as well as in model skill at simulating $[Nd]_d$ and ε_{Nd} consistent with water column measurements. The magnitude of the benthic flux and riverine source scaling influence model $[Nd]_d$ variability under low scavenging efficiencies.

815

In line with previous studies, the global Nd inventory in *REF* is 4.27×10^{12} g, owing to a global mean residence time of 727 years. Of the total Nd source to the ocean, 64% is apportioned to the seafloor benthic flux, 30% to riverine sources, and 6% to aeolian dust deposition. Our reference simulation captures the main features of the modern marine Nd cycle, although the ε_{Nd} signature of the Pacific is 3 to 4 ε_{Nd}-units too unradiogenic compared to seawater measurements, alluding to incongruent
820   dissolution of the bulk sediment and a likely favouring of interactions from radiogenic volcanic components of the seafloor sediment that may constitute spatially elevated benthic fluxes.

Model-data inconsistencies in some instances relate to the low resolution of FAMOUS preventing full resolution of surface point sources, which are highly variable in nature. Importantly, though, these inconsistencies disclose aspects of the global
825   marine Nd cycle to focus further detailed investigation. For example, including a better quantification of the modes and rates of scavenging, an improved understanding of Nd desorption, additional exploration of river particulates as a major global Nd source to seawater, and the need for spatial constraints on the isotopic signature and rates of a benthic flux; specifically, strong localised effects and the physical/environmental conditions driving elevated fluxes. The optimised simulation therefore forms a well-developed scheme designed to answer specific outstanding questions regarding the marine Nd cycle.

830

We performed idealised sensitivity studies using our optimised scheme to test three different mobile seafloor sediment ε_{Nd} distributions, investigating regions in the Atlantic and Pacific where more extreme and highly reactive sediment ε_{Nd} phases (relative to the bulk) may be preferentially contributing ε_{Nd} to the pore water and thus seawater via early diagenetic processes. This in part attempts to broadly elucidate to a first order what the dominant labile ε_{Nd} signals of the sediment (effective
835   sedimentary Nd release) are under a seafloor-wide benthic flux driven model of marine Nd cycling, paving the way towards a more mechanistic global model of the sedimentary Nd budget to seawater. Model skill for ε_{Nd} improved globally under a seafloor Nd source that regionally enhanced reactive sediment phases; for example, preferential mobilisation of highly radiogenic volcanic components of detrital sediment in the equatorial Pacific can partially explain the radiogenic change in Pacific deep water along its sluggish northward flow path. However, model-data offsets in intermediate layers of the Pacific
840   demonstrate that localised marginal volcanic sediment sources likely pose a larger and more distinct Nd source, as opposed to abyssal seafloor sediment. The weak sensitivity of NADW to localised highly unradiogenic detrital sources where water mass mixing governs deep seawater ε_{Nd} distributions, suggests that an abyssal benthic flux is of secondary importance in determining the modern deep Atlantic ε_{Nd}. Seawater here is more likely influenced by the larger and more distinct reactive unradiogenic surface and marginal Nd sources in proximity to regions of direct continental weathering around key convection sites. In a
845   final sensitivity experiment exploring the response of seawater ε_{Nd} to a continental margin constrained versus a seafloor-wide benthic flux, we demonstrate that modern bottom waters within the Pacific Ocean are sensitive to non-conservative alterations resulting from an abyssal benthic flux, whilst the North Atlantic displays a limited expression of such effects.

Fundamentally this study demonstrates that despite over a decade of increasing efforts to constrain and describe the global
850 marine Nd cycle within complex sophisticated global models, a global framework is limited. Poor quantifications of non-conservative sediment-water interactions limits the capability of global models to fully resolve end member ε_{Nd} signals, with model-data offsets sometimes larger than the ε_{Nd} shifts observed in the palaeoceanographic records. Such errors limit the capability of global Nd isotope models to precisely resolve what climatic or oceanographic conditions may be driving such deviations in seawater ε_{Nd}, particularly in untangling complex processes during periods when global weathering regimes and/or
855 ocean circulation convection rates are largely unconstrained. Moreover, it is becoming increasingly transparent that there are distinct regional differences in how modern seawater acquires its ε_{Nd} signal, in part relating to the interplay of Nd addition and water advection rates. Moving forwards, regional models, that can better encompass measured seawater Nd profiles, and provide more complex spatiotemporal representations of Nd source/sink distributions, may be better positioned to reconcile the marine Nd cycle and for palaeoceanographic applications.

860

In closing, this study illustrates that although a benthic flux is an important Nd source to seawater, and that it can describe key features of the modern marine Nd cycle, perhaps too much emphasis has recently been placed upon exclusively resolving non-conservative interactions of an abyssal deep seafloor flux to solve the Nd paradox. We recommend future studies to continue to explore marine Nd cycling in a holistic way, advancing constraints on the processes, characteristics, and spatial variability
865 of all major sediment-water interactions. This should include a particular focus on those processes influencing seawater ε_{Nd} at intermediate depths, with the purpose of reliably predicting localised non-conservative effects and highlighting where they dominate seawater ε_{Nd} distributions in the deep ocean. Within such a framework, and under the recent ever-increasing momentum of studies seeking to resolve the marine Nd cycle, we can edge closer to unlocking the full potential of Nd isotopes as an oceanographic and climatic tracer.

870 **Code availability**

The base code for FAMOUS is protected under UK Crown Copyright and can be obtained from National Centre for Atmospheric Science (NCAS) Computational Modelling Services (CMS): https://cms.ncas.ac.uk/miscellaneous/um-famous/ (last accessed: 14th September 2022). The code detailing the Nd isotope scheme (ND v1.0) in FAMOUS is associated with Robinson et al. (submitted) and is available from the Research Data Leeds Repository (Robinson
875 2022a: https://doi.org/10.5518/1136), under a Creative Commons Attribution 4.0 International (CCBY 4.0) license. These files are known as code modification (i.e. 'mod') files and should be applied to the original base code for the model. The files and corresponding information that needs to be applied to configure the different simulations presented in this manuscript are available from the Research Data Leeds Repository (Robinson et al., 2022b; https://doi.org/10.5518/1181).

880 Reference simulations from the Nd isotope scheme optimisation

- XPIAB *reference ('REF') simulation* (0-6,000 years)
- XPIAD *Nd concentration reference ('REF_CONC1') simulation* (0-6,000 years)
- XPHJF *Nd concentration reference; best performing from parameter analysis ('REF_CONC2') simulation* (0-6,000 years)
885 - XPIAC *Nd isotope reference ('REF_IC') simulation* (0-6,000 years)

Seafloor sediment Nd isotope distribution sensitivity simulations
- XPIAG *reference ('REF_SED2') simulation* (0-6,000 years)
- XPIAH *reference ('REF_SED3') simulation* (0-6,000 years)
890

Continental margin constrained benthic flux sensitivity simulation
- XPIAQ *reference ('REF_SED3_MG') simulation* (0-6,000 years)

Data availability

The data are available via the Research Data Leeds Repository (Robinson 2022: https://doi.org/10.5518/1181)

895 **Supplementary Information**

The supplement related to this article is to be associated with a DOI, and currently attached as a .zip (Supplementary_Robinson.et.al_inPrep.zip), containing:

Supplementary Information: Documented supplementary text, figures and tables (Figures S1-S10, Table S2, and Text S1)

Table S1: Parameter values and the resulting marine Nd inventory ($Nd(I)$) and residence time (τ_{Nd}) for all the simulations
900 forming the optimisation of the Nd isotope scheme in FAMOUS

simulation_files/: Folder with all the simulation files needed to run each simulation

Author contribution

SMR, RFI and LJG conceived of the study and the overall approach to each component of it. SMR designed and ran the optimisation and sensitivity simulations, with technical input from RFI and LJG. LA constructed the Gaussian Process
905 emulator utilised to optimise the scheme, with model results and technical scientific guidance provided by SMR. SMR produced the manuscript with input from all co-authors. All co-authors contributed scientific expertise throughout.

Competing interests

The authors declare that they have no conflict of interest

Acknowledgements

910   SMR was funded by the Natural Environment Research Council (NERC) SPHERES Doctoral Training Partnership (grant number: NE/ L002574/1). LJG was funded by UKRI Future Leaders Fellowship 'SMBGen' (grant number: MR/S016961/1). FP was supported by the European Union's Horizon 2020 program (grant number: 101023443). TvdF acknowledges funding from the NERC grant NE/ P019080/1. LCA was funded by the ARC ITRH for Transforming energy Infrastructure through Digital Engineering (TIDE, Grant No. IH200100009).

915   **References**

Abbott, A. N.: A benthic flux from calcareous sediments results in non-conservative neodymium behavior during lateral transport: A study from the Tasman Sea, Geology, 47, 363–366, https://doi.org/10.1130/g45904.1, 2019.

Abbott, A. N., Haley, B. A., and McManus, J.: Bottoms up: Sedimentary control of the deep North Pacific Ocean's εNd signature, Geology, 43, 1035–1038, https://doi.org/10.1130/G37114.1, 2015a.

920   Abbott, A. N., Haley, B. A., McManus, J., and Reimers, C. E.: The sedimentary flux of dissolved rare earth elements to the ocean, Geochim. Cosmochim. Acta, 154, 186–200, https://doi.org/10.1016/j.gca.2015.01.010, 2015b.

Abbott, A. N., Haley, B. A., and McManus, J.: The impact of sedimentary coatings on the diagenetic Nd flux, Earth Planet. Sci. Lett., 449, 217–227, https://doi.org/10.1016/j.epsl.2016.06.001, 2016.

Abbott, A. N., Löhr, S., and Trethewy, M.: Are clay minerals the primary control on the oceanic rare earth element budget?, 925   Front. Mar. Sci., 6, 1–19, https://doi.org/10.3389/fmars.2019.00504, 2019.

Abbott, A. N., Löhr, S. C., Payne, A., Kumar, H., and Du, J.: Widespread lithogenic control of marine authigenic neodymium isotope records? Implications for paleoceanographic reconstructions, Geochim. Cosmochim. Acta, 319, 318–336, https://doi.org/10.1016/j.gca.2021.11.021, 2022.

Amakawa, H., Sasaki, K., and Ebihara, M.: Nd isotopic composition in the central North Pacific, Geochim. Cosmochim. Acta, 930   73, 4705–4719, https://doi.org/10.1016/j.gca.2009.05.058, 2009.

Arsouze, T., Dutay, J.-C. C., Lacan, F., and Jeandel, C.: Modeling the neodymium isotopic composition with a global ocean circulation model, Chem. Geol., 239, 165–177, https://doi.org/10.1016/j.chemgeo.2006.12.006, 2007.

Arsouze, T., Dutay, J. C., Lacan, F., and Jeandel, C.: Reconstructing the Nd oceanic cycle using a coupled dynamical-Biogeochemical model, 6, 2829–2846, https://doi.org/10.5194/bg-6-2829-2009, 2009.

935   Astfalck, L. C., Cripps, E. J., Gosling, J. P., and Milne, I. A.: Emulation of vessel motion simulators for computationally efficient uncertainty quantification, Ocean Eng., 172, 726–736, https://doi.org/10.1016/j.oceaneng.2018.11.059, 2019.

Bacon, M. P. and Anderson, R. F.: Distribution of Thorium Isotopes Between Dissolved and Particulate Forms in the Deep Sea, J. Geophys. Res., 87, 2045–2056, https://doi.org/10.1029/JC087iC03p02045, 1982.

Basak, C., Pahnke, K., Frank, M., Lamy, F., and Gersonde, R.: Neodymium isotopic characterization of Ross Sea Bottom 940   Water and its advection through the southern South Pacific, Earth Planet. Sci. Lett., 419, 211–221,

https://doi.org/10.1016/j.epsl.2015.03.011, 2015.

Bayon, G., German, C. R., Burton, K. W., Nesbitt, R. W., and Rogers, N.: Sedimentary Fe-Mn oxyhydroxides as paleoceanographic archives and the role of aeolian flux in regulating oceanic dissolved REE, Earth Planet. Sci. Lett., 224, 477–492, https://doi.org/10.1016/j.epsl.2004.05.033, 2004.

945 Behrens, M. K., Pahnke, K., Schnetger, B., and Brumsack, H. J.: Sources and processes affecting the distribution of dissolved Nd isotopes and concentrations in the West Pacific, Geochim. Cosmochim. Acta, 222, 508–534, https://doi.org/10.1016/j.gca.2017.11.008, 2018.

Bertram, C. J. and Elderfield, H.: The geochemical balance of the rare earth elements and neodymium isotopes in the oceans, Geochim. Cosmochim. Acta, 57, 1957–1986, https://doi.org/10.1016/0016-7037(93)90087-D, 1993.

950 Blanchet, C. L.: A database of marine and terrestrial radiogenic Nd and Sr isotopes for tracing earth-surface processes, Earth Syst. Sci. Data, 11, 741–759, https://doi.org/10.5194/essd-11-741-2019, 2019.

Blaser, P., Lippold, J., Gutjahr, M., Frank, N., Link, J. M., and Frank, M.: Extracting foraminiferal seawater Nd isotope signatures from bulk deep sea sediment by chemical leaching, Chem. Geol., 439, 189–204, https://doi.org/10.1016/j.chemgeo.2016.06.024, 2016.

955 Blaser, P., Frank, M., and van de Flierdt, T.: Revealing past ocean circulation with neodymium isotopes, Past Glob. Chang. Mag., 27, 54–55, https://doi.org/10.22498/pages.27.2.54, 2019a.

Blaser, P., Pöppelmeier, F., Schulz, H., Gutjahr, M., Frank, M., Lippold, J., Heinrich, H., Link, J. M., Hoffmann, J., Szidat, S., and Frank, N.: The resilience and sensitivity of Northeast Atlantic deep water εNd to overprinting by detrital fluxes over the past 30,000 years, Geochim. Cosmochim. Acta, 245, 79–97, https://doi.org/10.1016/j.gca.2018.10.018, 2019b.

960 Byrne, R. H. and Kim, K. H.: Rare earth element scavenging in seawater, Geochim. Cosmochim. Acta, 54, 2645–2656, https://doi.org/10.1016/0016-7037(90)90002-3, 1990.

Chamecki, M., Chor, T., Yang, D., and Meneveau, C.: Material Transport in the Ocean Mixed Layer: Recent Developments Enabled by Large Eddy Simulations, https://doi.org/10.1029/2019RG000655, 2019.

Chebyshev, P.: Des valeurs moyennes, J. Math. Pures Appl., 12, 177–184, 1867.

965 Dausmann, V., Frank, M., Gutjahr, M., and Rickli, J.: Glacial reduction of AMOC strength and long-term transition in weathering inputs into the Southern Ocean since the mid-Miocene: Evidence from radiogenic Nd and Hf isotopes, Paleoceanography, 32, 265–283, https://doi.org/10.1002/2016PA003056, 2017.

Dentith, J. E., Ivanovic, R. F., Gregoire, L. J., Tindall, J. C., and Smith, R. S.: Ocean circulation drifts in multi-millennial climate simulations: the role of salinity corrections and climate feedbacks, Clim. Dyn., 52, 1761–1781, 970 https://doi.org/10.1007/s00382-018-4243-y, 2019.

Dentith, J. E., Ivanovic, R. F., Gregoire, L. J., Tindall, J. C., and Robinson, L. F.: Simulating stable carbon isotopes in the ocean component of the FAMOUS general circulation model with MOSES1 (XOAVI), Geosci. Model Dev., 13, 3529–3552, https://doi.org/10.5194/gmd-13-3529-2020, 2020.

Du, J., Haley, B. A., and Mix, A. C.: Neodymium isotopes in authigenic phases, bottom waters and detrital sediments in the 975 Gulf of Alaska and their implications for paleo-circulation reconstruction, Geochim. Cosmochim. Acta, 193, 14–35, https://doi.org/10.1016/j.gca.2016.08.005, 2016.

Du, J., Haley, B. A., Mix, A. C., Walczak, M. H., and Praetorius, S. K.: Flushing of the deep Pacific Ocean and the deglacial rise of atmospheric CO2 concentrations, Nat. Geosci., 11, 749–755, https://doi.org/10.1038/s41561-018-0205-6, 2018.

Du, J., Haley, B. A., and Mix, A. C.: Evolution of the Global Overturning Circulation since the Last Glacial Maximum based 980 on marine authigenic neodymium isotopes, Quat. Sci. Rev., 241, 106396, https://doi.org/10.1016/j.quascirev.2020.106396, 2020.

Essery, R. L. H., Best, M. J., and Cox, P. M.: MOSES 2.2 technical documentation. Hadley Centre Technical Note 30, 2001.

Essery, R. L. H., Best, M. J., Betts, R. A., Cox, P. M., and Taylor, C. M.: Explicit representation of subgrid heterogeneity in a GCM land surface scheme, J. Hydrometeorol., 4, 530–543, https://doi.org/10.1175/1525-7541(2003)004<0530:EROSHI>2.0.CO;2, 2003.

Flato, G., Marotzke, J., Abiodun, B., Braconnot, P., Sin Chan Chou, Collins, W., Cox, P., Driouech, F., Emori, S., Eyring, V., Forest, C., Gleckler, P., Guilyardi, E., Jakob, C., Kattsov, V., Reason, C., and Rummukainen, M.: Evaluation of climate models, Climate Change 2013 the Physical Science Basis: Working Group I Contribution to the Fifth Assessment Report of the Intergovernmental Panel on Climate Change, Cambridge University Press, Cambridge, United Kingdom and New York, NY, USA., 741–866 pp., https://doi.org/10.1017/CBO9781107415324.020, 2013.

van de Flierdt, T. and Frank, M.: Neodymium isotopes in paleoceanography, Quat. Sci. Rev., 29, 2439–2441, https://doi.org/10.1016/j.quascirev.2010.07.001, 2010.

van de Flierdt, T., Frank, M., Lee, D. C., Halliday, A. N., Reynolds, B. C., and Hein, J. R.: New constraints on the sources and behavior of neodymium and hafnium in seawater from Pacific Ocean ferromanganese crusts, Geochim. Cosmochim. Acta, 68, 3827–3843, https://doi.org/10.1016/j.gca.2004.03.009, 2004.

van de Flierdt, T., Pahnke, K., Amakawa, H., Andersson, P., Basak, C., Coles, B., Colin, C., Crocket, K., Frank, M., Frank, N., Goldstein, S. L., Goswami, V., Haley, B. A., Hathorne, E. C., Hemming, S. R., Henderson, G. M., Jeandel, C., Jones, K., Kreissig, K., Lacan, F., Lambelet, M., Martin, E. E., Newkirk, D. R., Obata, H., Pena, L., Piotrowski, A. M., Pradoux, C., Scher, H. D., Schöberg, H., Singh, S. K., Stiche, T., Tazoe, H., Vance, D., and Yang, J.: GEOTRACES intercalibration of neodymium isotopes and rare earth element concentrations in seawater and suspended particles. Part 1: Reproducibility of results for the international intercomparison, Limnol. Oceanogr. Methods, 10, 234–251, https://doi.org/10.4319/lom.2012.10.234, 2012.

van de Flierdt, T., Grifths, A. M., Lambelet, M., Little, S. H., Stichel, T., and Wilson, D. J.: Neodymium in the oceans: A global database, a regional comparison and implications for palaeoceanographic research, https://doi.org/10.1098/rsta.2015.0293, 2016.

Frank, M.: Radiogenic isotopes: Tracers of past ocean circulation and erosional input, Rev. Geophys., 40, 1001, https://doi.org/10.1029/2000RG000094, 2002.

Fröllje, H., Pahnke, K., Schnetger, B., Brumsack, H. J., Dulai, H., and Fitzsimmons, J. N.: Hawaiian imprint on dissolved Nd and Ra isotopes and rare earth elements in the central North Pacific: Local survey and seasonal variability, Geochim. Cosmochim. Acta, 189, 110–131, https://doi.org/10.1016/j.gca.2016.06.001, 2016.

Fuhr, M., Laukert, G., Yu, Y., Nürnberg, D., and Frank, M.: Tracing Water Mass Mixing From the Equatorial to the North Pacific Ocean With Dissolved Neodymium Isotopes and Concentrations, Front. Mar. Sci., 7, 1261, https://doi.org/10.3389/fmars.2020.603761, 2021.

GEOTRACES Intermediate Data Product Group: The GEOTRACES Intermediate Data Product 2021 (IDP2021), https://doi.org/5/cf2d9ba9-d51d-3b7c-e053-8486abc0f5fd, 2021.

Goldstein, S. J. and Jacobsen, S. B.: The Nd and Sr isotopic systematics of river-water dissolved material: Implications for the sources of Nd and Sr in seawater, Chemical Geology (Isotope Geoscience Section), 245–272 pp., https://doi.org/10.1016/0168-9622(87)90045-5, 1987.

Goldstein, S. J. and Jacobsen, S. B.: Rare earth elements in river waters, Earth Planet. Sci. Lett., 89, 35–47, https://doi.org/10.1016/0012-821X(88)90031-3, 1988.

Goldstein, S. L. and Hemming, S. R.: Long-lived Isotopic Tracers in Oceanography, Paleoceanography, and Ice-Sheet Dynamics, 453–483, https://doi.org/10.1016/B0-08-043751-6/06179-X, 2003.

Gordon, C., Cooper, C., Senior, C. A., Banks, H., Gregory, J. M., Johns, T. C., Mitchell, J. F. B., and Wood, R. A.: The simulation of SST, sea ice extents and ocean heat transports in a version of the Hadley Centre coupled model without flux adjustments, Clim. Dyn., 16, 147–168, https://doi.org/10.1007/s003820050010, 2000.

Gregoire, L. J., Valdes, P. J., Payne, A. J., and Kahana, R.: Optimal tuning of a GCM using modern and glacial constraints, Clim. Dyn., 37, 705–719, https://doi.org/10.1007/s00382-010-0934-8, 2011.

Gregoire, L. J., Payne, A. J., and Valdes, P. J.: Deglacial rapid sea level rises caused by ice-sheet saddle collapses, Nature, 487, 219–222, https://doi.org/10.1038/nature11257, 2012.

1030 Gregoire, L. J., Valdes, P. J., and Payne, A. J.: The relative contribution of orbital forcing and greenhouse gases to the North American deglaciation, Geophys. Res. Lett., 42, 9970–9979, https://doi.org/10.1002/2015GL066005, 2015.

Grenier, M., Jeandel, C., Lacan, F., Vance, D., Venchiarutti, C., Cros, A., and Cravatte, S.: From the subtropics to the central equatorial Pacific Ocean: Neodymium isotopic composition and rare earth element concentration variations, J. Geophys. Res. Ocean., 118, 592–618, https://doi.org/10.1029/2012JC008239, 2013.

1035 Grousset, F. E., Parra, M., Bory, A., Martinez, P., Bertrand, P., Shimmield-M, G., and Ellamn, R. M.: Saharan Wind Regimes Traced by the Sr-Nd Isotopic Composition of Subtropical Atlantic Sediments: Last Glacial Maximum vs Today, Quaternary Science Reviews, 395–409 pp., https://doi.org/https://doi.org/10.1016/S0277-3791(97)00048-6, 1998.

Gu, S., Liu, Z., Jahn, A., Rempfer, J., Zhang, J., and Joos, F.: Modeling Neodymium Isotopes in the Ocean Component of the Community Earth System Model (CESM1), J. Adv. Model. Earth Syst., 11, 624–640, https://doi.org/10.1029/2018MS001538, 1040 2019.

Gutjahr, M., Frank, M., Stirling, C. H., Keigwin, L. D., and Halliday, A. N.: Tracing the Nd isotope evolution of North Atlantic Deep and Intermediate Waters in the western North Atlantic since the Last Glacial Maximum from Blake Ridge sediments, Earth Planet. Sci. Lett., 266, 61–77, https://doi.org/10.1016/j.epsl.2007.10.037, 2008.

Haley, B. A., Klinkhammer, G. P., and McManus, J.: Rare earth elements in pore waters of marine sediments, Geochim. 1045 Cosmochim. Acta, 68, 1265–1279, https://doi.org/10.1016/j.gca.2003.09.012, 2004.

Haley, B. A., Du, J., Abbott, A. N., and McManus, J.: The Impact of Benthic Processes on Rare Earth Element and Neodymium Isotope Distributions in the Oceans, Front. Mar. Sci., 4, 426, https://doi.org/10.3389/fmars.2017.00426, 2017.

Haley, B. A., Wu, Y., Muratli, J. M., Basak, C., Pena, L. D., and Goldstein, S. L.: Rare earth element and neodymium isotopes of the eastern US GEOTRACES Equatorial Pacific Zonal Transect (GP16), Earth Planet. Sci. Lett., 576, 117233, 1050 https://doi.org/10.1016/j.epsl.2021.117233, 2021.

Homoky, W. B., Weber, T., Berelson, W. M., Conway, T. M., Henderson, G. M., Van Hulten, M., Jeandel, C., Severmann, S., and Tagliabue, A.: Quantifying trace element and isotope fluxes at the ocean-sediment boundary: A review, Philos. Trans. R. Soc. A, 374, https://doi.org/10.1098/rsta.2016.0246, 2016.

Howe, J. N. W., Piotrowski, A. M., Hu, R., and Bory, A.: Reconstruction of east–west deep water exchange in the low latitude 1055 Atlantic Ocean over the past 25,000 years, Earth Planet. Sci. Lett., 458, 327–336, https://doi.org/10.1016/j.epsl.2016.10.048, 2017.

Hu, R. and Piotrowski, A. M.: Neodymium isotope evidence for glacial-interglacial variability of deepwater transit time in the Pacific Ocean, Nat. Commun., 9, 1–12, https://doi.org/10.1038/s41467-018-07079-z, 2018.

Jacobsen, S. B. and Wasserburg, G. J.: Sm-Nd evolution of chondrites, Earth Planet. Sci. Lett., 50, 139–155, 1060 https://doi.org/10.1016/0012-821X(80)90125-9, 1980.

Jeandel, C.: Overview of the mechanisms that could explain the "Boundary Exchange" at the land-ocean contact, https://doi.org/10.1098/rsta.2015.0287, 2016.

Jeandel, C. and Oelkers, E. H.: The influence of terrigenous particulate material dissolution on ocean chemistry and global element cycles, https://doi.org/10.1016/j.chemgeo.2014.12.001, 2015.

1065 Johannesson, K. H. and Burdige, D. J.: Balancing the global oceanic neodymium budget: Evaluating the role of groundwater, Earth Planet. Sci. Lett., 253, 129–142, https://doi.org/10.1016/j.epsl.2006.10.021, 2007.

Jones, C., Gregory, J., Thorpe, R., Cox, P., Murphy, J., Sexton, D., and Valdes, P.: Systematic optimisation and climate

simulation of FAMOUS, a fast version of HadCM3, Clim. Dyn., 25, 189–204, https://doi.org/10.1007/s00382-005-0027-2, 2005.

1070 Jones, K. M., Khatiwala, S. P., Goldstein, S. L., Hemming, S. R., and van de Flierdt, T.: Modeling the distribution of Nd isotopes in the oceans using an ocean general circulation model, Earth Planet. Sci. Lett., 272, 610–619, https://doi.org/10.1016/j.epsl.2008.05.027, 2008.

Jonkers, L., Zahn, R., Thomas, A., Henderson, G., Abouchami, W., François, R., Masque, P., Hall, I. R., and Bickert, T.: Deep circulation changes in the central South Atlantic during the past 145 kyrs reflected in a combined231Pa/230Th, Neodymium
1075 isotope and benthic δC13 record, Earth Planet. Sci. Lett., 419, 14–21, https://doi.org/10.1016/j.epsl.2015.03.004, 2015.

Kennedy, M. C. and O'Hagan, A.: Bayesian calibration of computer models, J. R. Stat. Soc. Ser. B Stat. Methodol., 63, 425–464, https://doi.org/10.1111/1467-9868.00294, 2001.

Lacan, F. and Jeandel, C.: Acquisition of the neodymium isotopic composition of the North Atlantic Deep Water, Geochemistry, Geophys. Geosystems, 6, https://doi.org/10.1029/2005GC000956, 2005a.

1080 Lacan, F. and Jeandel, C.: Neodymium isotopes as a new tool for quantifying exchange fluxes at the continent-ocean interface, Earth Planet. Sci. Lett., 232, 245–257, https://doi.org/10.1016/j.epsl.2005.01.004, 2005b.

Lagarde, M., Lemaitre, N., Planquette, H., Grenier, M., Belhadj, M., Lherminier, P., and Jeandel, C.: Particulate Rare Earth Element behavior in the North Atlantic (GEOVIDE cruise), Biogeosciences Discuss., 1–32, https://doi.org/10.5194/bg-2019-462, 2020.

1085 Lambelet, M., van de Flierdt, T., Crocket, K., Rehkämper, M., Kreissig, K., Coles, B., Rijkenberg, M. J. A., Gerringa, L. J. A., de Baar, H. J. W., and Steinfeldt, R.: Neodymium isotopic composition and concentration in the western North Atlantic Ocean: Results from the GEOTRACES GA02 section, Geochim. Cosmochim. Acta, 177, 1–29, https://doi.org/10.1016/j.gca.2015.12.019, 2016.

Lambelet, M., van de Flierdt, T., Butler, E. C. V., Bowie, A. R., Rintoul, S. R., Watson, R. J., Remenyi, T., Lannuzel, D.,
1090 Warner, M., Robinson, L. F., Bostock, H. C., and Bradtmiller, L. I.: The Neodymium Isotope Fingerprint of Adélie Coast Bottom Water, Geophys. Res. Lett., 45, 11,247-11,256, https://doi.org/10.1029/2018GL080074, 2018.

Lippold, J., Gutjahr, M., Blaser, P., Christner, E., de Carvalho Ferreira, M. L., Mulitza, S., Christl, M., Wombacher, F., Böhm, E., Antz, B., Cartapanis, O., Vogel, H., and Jaccard, S. L.: Deep water provenance and dynamics of the (de)glacial Atlantic meridional overturning circulation, Earth Planet. Sci. Lett., 445, 68–78, https://doi.org/10.1016/j.epsl.2016.04.013, 2016.

1095 Martin, E. E. and Scher, H. D.: Preservation of seawater Sr and Nd isotopes in fossil fish teeth: Bad news and good news, Earth Planet. Sci. Lett., 220, 25–39, https://doi.org/10.1016/S0012-821X(04)00030-5, 2004.

Morrison, R., Waldner, A., Hathorne, E. C., Rahlf, P., Zieringer, M., Montagna, P., Colin, C., Frank, N., and Frank, M.: Limited influence of basalt weathering inputs on the seawater neodymium isotope composition of the northern Iceland Basin, Chem. Geol., 511, 358–370, https://doi.org/10.1016/j.chemgeo.2018.10.019, 2019.

1100 Noh, Y., Kang, I. S., Herold, M., and Raasch, S.: Large eddy simulation of particle settling in the ocean mixed layer, Phys. Fluids, 18, 85109, https://doi.org/10.1063/1.2337098, 2006.

Oka, A., Tazoe, H., and Obata, H.: Simulation of global distribution of rare earth elements in the ocean using an ocean general circulation model, J. Oceanogr., 1, 3, https://doi.org/10.1007/s10872-021-00600-x, 2021.

Osborne, A. H., Haley, B. A., Hathorne, E. C., Plancherel, Y., and Frank, M.: Rare earth element distribution in Caribbean
1105 seawater: Continental inputs versus lateral transport of distinct REE compositions in subsurface water masses, Mar. Chem., 177, 172–183, https://doi.org/10.1016/j.marchem.2015.03.013, 2015.

Osborne, A. H., Hathorne, E. C., Schijf, J., Plancherel, Y., Boning, P., and Frank, M.: The potential of sedimentary foraminiferal rare earth element patterns to trace water masses in the past, Geochemistry Geophys. Geosystems, 18, 1–26, https://doi.org/10.1002/2016GC006782, 2017.

Paffrath, R., Pahnke, K., Böning, P., Rutgers van der Loeff, M., Valk, O., Gdaniec, S., and Planquette, H.: Seawater-Particle Interactions of Rare Earth Elements and Neodymium Isotopes in the Deep Central Arctic Ocean, J. Geophys. Res. Ocean., 126, e2021JC017423, https://doi.org/10.1029/2021JC017423, 2021.

Pahnke, K., van de Flierdt, T., Jones, K. M., Lambelet, M., Hemming, S. R., and Goldstein, S. L.: GEOTRACES intercalibration of neodymium isotopes and rare earth element concentrations in seawater and suspended particles. Part 2: Systematic tests and baseline profiles, Limnol. Oceanogr. Methods, 10, 252–269, https://doi.org/10.4319/lom.2012.10.252, 2012.

Pasquier, B., Hines, S. K. V, Liang, H., Wu, Y., and John, S. G.: GNOM v1 . 0 : An optimized steady-state model of the modern marine neodymium cycle, Geosci. Model Dev., 147, 2021.

Pearce, C. R., Jones, M. T., Oelkers, E. H., Pradoux, C., and Jeandel, C.: The effect of particulate dissolution on the neodymium (Nd) isotope and Rare Earth Element (REE) composition of seawater, Earth Planet. Sci. Lett., 369–370, 138–147, https://doi.org/10.1016/j.epsl.2013.03.023, 2013.

Piotrowski, A. M., Goldstein, S. L., Hemming, S. R., and Fairbanks, R. G.: Intensification and variability of ocean thermohaline circulation through the last deglaciation, Earth Planet. Sci. Lett., 225, 205–220, https://doi.org/10.1016/j.epsl.2004.06.002, 2004.

Piotrowski, A. M., Galy, A., Nicholl, J. A. L., Roberts, N., Wilson, D. J., Clegg, J. A., and Yu, J.: Reconstructing deglacial North and South Atlantic deep water sourcing using foraminiferal Nd isotopes, Earth Planet. Sci. Lett., 357–358, 289–297, https://doi.org/10.1016/j.epsl.2012.09.036, 2012.

Pöppelmeier, F., Scheen, J., Blaser, P., Lippold, J., Gutjahr, M., and Stocker, T. F.: Influence of Elevated Nd Fluxes on the Northern Nd Isotope End Member of the Atlantic During the Early Holocene, Paleoceanogr. Paleoclimatology, 35, e2020PA003973, https://doi.org/10.1029/2020PA003973, 2020a.

Pöppelmeier, F., Blaser, P., Gutjahr, M., Jaccard, S. L., Frank, M., Max, L., and Lippold, J.: Northern Sourced Water dominated the Atlantic Ocean during the Last Glacial Maximum, Geology, 48, https://doi.org/10.1130/G47628.1, 2020b.

Pöppelmeier, F., Lippold, J., Blaser, P., Gutjahr, M., Frank, M., and Stocker, T. F.: Neodymium isotopes as a paleo-water mass tracer: A model-data reassessment, Quat. Sci. Rev., 279, 107404, https://doi.org/10.1016/J.QUASCIREV.2022.107404, 2022.

Rahlf, P., Hathorne, E., Laukert, G., Gutjahr, M., Weldeab, S., and Frank, M.: Tracing water mass mixing and continental inputs in the southeastern Atlantic Ocean with dissolved neodymium isotopes, Earth Planet. Sci. Lett., 530, 115944, https://doi.org/10.1016/j.epsl.2019.115944, 2020.

Rahlf, P., Laukert, G., Hathorne, E. C., Vieira, L. H., and Frank, M.: Dissolved neodymium and hafnium isotopes and rare earth elements in the Congo River Plume: Tracing and quantifying continental inputs into the southeast Atlantic, Geochim. Cosmochim. Acta, 294, 192–214, https://doi.org/10.1016/j.gca.2020.11.017, 2021.

Rasmussen, C. E. and Williams, C. K. I.: Gaussian processes for machine learning., https://doi.org/10.1142/S0129065704001899, 2006.

Rempfer, J., Stocker, T. F., Joos, F., Dutay, J.-C., and Siddall, M.: Modelling Nd-isotopes with a coarse resolution ocean circulation model: Sensitivities to model parameters and source/sink distributions, Geochim. Cosmochim. Acta, 75, 5927–5950, https://doi.org/10.1016/j.gca.2011.07.044, 2011.

Rempfer, J., Stocker, T. F., Joos, F., and Dutay, J. C.: On the relationship between Nd isotopic composition and ocean overturning circulation in idealized freshwater discharge events, Paleoceanography, 27, PA3211, https://doi.org/10.1029/2012PA002312, 2012.

Roberts, N. L., Piotrowski, A. M., McManus, J. F., and Keigwin, L. D.: Synchronous deglacial overturning and water mass source changes, Science (80-.)., 327, 75–78, https://doi.org/10.1126/science.1178068, 2010.

Robinson, S., Ivanovic, R., van de Flierdt, T., Blanchet, C. L., Tachikawa, K., Martin, E. E., Cook, C. P., Williams, T., Gregoire, L., Plancherel, Y., Jeandel, C., and Arsouze, T.: Global continental and marine detrital εNd: An updated compilation

for use in understanding marine Nd cycling, Chem. Geol., 567, 120119, https://doi.org/10.1016/j.chemgeo.2021.120119, 2021.

Robinson, S., Ivanovic, R. F., Gregoire, L. J., Tindall, J. C., van de Flierdt, T., Plancherel, Y., Pöppelmeier, F., Tachikawa, K., and Valdes, P. J.: Simulating neodymium isotopes in the ocean component of the FAMOUS general circulation model (XPDAA): sensitivities to reversible scavenging efficiency and benthic source distributions, [Manuscript submitted for publication], n.d.

Rousseau, T. C. C., Sonke, J. E., Chmeleff, J., Van Beek, P., Souhaut, M., Boaventura, G., Seyler, P., and Jeandel, C.: Rapid neodymium release to marine waters from lithogenic sediments in the Amazon estuary, Nat. Commun., 6, https://doi.org/10.1038/ncomms8592, 2015.

Siddall, M., Khatiwala, S., van de Flierdt, T., Jones, K., Goldstein, S. L., Hemming, S., and Anderson, R. F.: Towards explaining the Nd paradox using reversible scavenging in an ocean general circulation model, Earth Planet. Sci. Lett., 274, 448–461, https://doi.org/10.1016/j.epsl.2008.07.044, 2008.

Smith, R. S.: The FAMOUS climate model (versions XFXWB and XFHCC): Description update to version XDBUA, Geosci. Model Dev., 5, 269–276, https://doi.org/10.5194/gmd-5-269-2012, 2012.

Smith, R. S. and Gregory, J. M.: A study of the sensitivity of ocean overturning circulation and climate to freshwater input in different regions of the North Atlantic, Geophys. Res. Lett., 36, L15701, https://doi.org/10.1029/2009GL038607, 2009.

Smith, R. S., Gregory, J. M., and Osprey, A.: A description of the FAMOUS (version XDBUA) climate model and control run, Geosci. Model Dev., 1, 53–68, https://doi.org/10.5194/gmd-1-53-2008, 2008.

Stichel, T., Frank, M., Rickli, J., and Haley, B. A.: The hafnium and neodymium isotope composition of seawater in the Atlantic sector of the Southern Ocean, Earth Planet. Sci. Lett., 317–318, 282–294, https://doi.org/10.1016/j.epsl.2011.11.025, 2012.

Stichel, T., Kretschmer, S., Geibert, W., Lambelet, M., Plancherel, Y., Rutgers van der Loeff, M., and van de Flierdt, T.: Particle–Seawater Interaction of Neodymium in the North Atlantic, ACS Earth Sp. Chem., https://doi.org/10.1021/acsearthspacechem.0c00034, 2020.

Tachikawa, K., Athias, V., and Jeandel, C.: Neodymium budget in the modern ocean and paleo-oceanographic implications, J. Geophys. Res., 108, 3254, https://doi.org/10.1029/1999JC000285, 2003.

Tachikawa, K., Arsouze, T., Bayon, G., Bory, A., Colin, C., Dutay, J. C., Frank, N., Giraud, X., Gourlan, A. T., Jeandel, C., Lacan, F., Meynadier, L., Montagna, P., Piotrowski, A. M., Plancherel, Y., Pucéat, E., Roy-Barman, M., and Waelbroeck, C.: The large-scale evolution of neodymium isotopic composition in the global modern and Holocene ocean revealed from seawater and archive data, Chem. Geol., 457, 131–148, https://doi.org/10.1016/j.chemgeo.2017.03.018, 2017.

Valdes, P. J., Armstrong, E., Badger, M. P. S., Bradshaw, C. D., Bragg, F., Crucifix, M., Davies-Barnard, T., Day, J., Farnsworth, A., Gordon, C., Hopcroft, P. O., Kennedy, A. T., Lord, N. S., Lunt, D. J., Marzocchi, A., Parry, L. M., Pope, V., Roberts, W. H. G., Stone, E. J., Tourte, G. J. L., and Williams, J. H. T.: The BRIDGE HadCM3 family of climate models: HadCM3@Bristol v1.0, Geosci. Model Dev., 10, 3715–3743, https://doi.org/10.5194/gmd-10-3715-2017, 2017.

Wang, R., Clegg, J. A., Scott, P. M., Larkin, C. S., Deng, F., Thomas, A. L., Zheng, X. Y., and Piotrowski, A. M.: Reversible scavenging and advection – Resolving the neodymium paradox in the South Atlantic, Geochim. Cosmochim. Acta, 314, 121–139, https://doi.org/10.1016/j.gca.2021.09.015, 2021.

Williams, J. H. T., Smith, R. S., Valdes, P. J., Booth, B. B. B., and Osprey, A.: Optimising the FAMOUS climate model: inclusion of global carbon cycling, Geosci. Model Dev., 6, 141–160, https://doi.org/10.5194/gmd-6-141-2013, 2013.

Williamson, D.: Exploratory ensemble designs for environmental models using k-extended Latin Hypercubes, Environmetrics, 26, 268–283, https://doi.org/10.1002/env.2335, 2015.

Williamson, D., Goldstein, M., Allison, L., Blaker, A., Challenor, P., Jackson, L., and Yamazaki, K.: History matching for exploring and reducing climate model parameter space using observations and a large perturbed physics ensemble, Clim. Dyn., 41, 1703–1729, https://doi.org/10.1007/s00382-013-1896-4, 2013.

Wilson, D. J., Piotrowski, A. M., Galy, A., and Clegg, J. A.: Reactivity of neodymium carriers in deep sea sediments: Implications for boundary exchange and paleoceanography, Geochim. Cosmochim. Acta, 109, 197–221, https://doi.org/10.1016/j.gca.2013.01.042, 2013.

1200   Wilson, D. J., Crocket, K. C., van de Flierdt, T., Robinson, L. F., and Adkins, J. F.: Dynamic intermediate ocean circulation in the North Atlantic during Heinrich Stadial 1: A radiocarbon and neodymium isotope perspective, Paleoceanography, 29, 1072–1093, https://doi.org/10.1002/2014PA002674, 2015.

Xie, R. C., Marcantonio, F., and Schmidt, M. W.: Reconstruction of intermediate water circulation in the tropical North Atlantic during the past 22,000 years, Geochim. Cosmochim. Acta, 140, 455–467, https://doi.org/10.1016/j.gca.2014.05.041, 2014.

1205   Zheng, X. Y., Plancherel, Y., Saito, M. A., Scott, P. M., and Henderson, G. M.: Rare earth elements (REEs) in the tropical South Atlantic and quantitative deconvolution of their non-conservative behavior, Geochim. Cosmochim. Acta, 177, 217–237, https://doi.org/10.1016/j.gca.2016.01.018, 2016.

1210